Chemical modification of nanocrystalline metal oxides: effect of the real structure and surface chemistry on the sensor properties

M. N. Rumyantseva [*] *and A. M. Gas´kov*

Department of Chemistry, M. V. Lomonosov Moscow State University,
1 Leninskie Gory, 119991 Moscow, Russian Federation.
Fax: +7 (495) 939 0998. E-mail: roum@inorg.chem.msu.ru, marinarum@mail.ru

The relationships between the composition, structure, chemistry of the surface, and sensor properties of nanocomposites SnO_2—M_nO_m ($M_nO_m = Fe_2O_3$, MoO_3, V_2O_5) obtained by chemical precipitation from solutions were analyzed. The relationships between the elemental and phase composition of the nanocomposites and the effect of the composition on the nanostructure and the acidic and oxidation properties of the nanocomposite surface were considered. The modification of the SnO_2 surface by other oxides makes it possible to control the type and density of the acid sites and the oxidation properties of the surface and to enhance the selectivity of the materials in the detection of various gases.

Key words: nanocrystalline oxides, SnO_2, Fe_2O_3, V_2O_5, MoO_3, nanocomposites, chemical modification, distribution of components, real structure, acidic properties of surface, catalytic properties, sensor properties.

Introduction

Considerable interest in tin dioxide arisen in the recent time is due to its multifunctional character. Tin dioxide is used for the construction of gas sensors, catalysts, optoelectronic converters, and transparent electrodes.[1—5]

The uniqueness of SnO_2 as a material for gas sensors is determined by a combination of its physical and chemical properties.[6—8] The electroconductivity of SnO_2 is very sensitive to the surface composition, which reversibly changes upon surface reactions of chemisorbed oxygen (O_2^-, O^{2-}, O^-) and the gas mixture components that occur on the surface at 100—500 °C. Important advantages of SnO_2 are its stability in air, relative cheapness, and simplicity of preparation in the ultradispersed state. A substantial drawback of SnO_2 is its low selectivity caused by the presence of a wide spectrum of adsorption sites on the surface, which prevents identification of the contribution of each type of molecules in the gas phase to the total electric signal. In investigations in the area of materials for semiconducting sensors, the main attention is given to an increase in the selectivity of these materials.

One of the ways for enhancing the selectivity of wide gap semiconducting oxides is the modification of their surfaces and involvement of the oxides in the preparation of complex nonhomogeneous systems (nanocomposites) by the introduction into a highly dispersed oxide matrix of catalytic additives such as Platinum Group metals (Pt, Pd, Ru, Rh) or oxide catalysts (Fe_2O_3, La_2O_3, Cr_2O_3, Co_3O_4, V_2O_5, NiO, CuO, MoO_3, CeO_2). Nanocomposites are systems built up of crystalline particles of nanometer size (3—30 nm) assembled in agglomerates where the modifier is distributed in a complex manner between the bulk and surface of crystalline grains of the major phase. Since in the nanocrystalline systems surface atoms make a considerable contribution to the interaction between the major phase and the modifier, it is impossible to predict the character of mutual distribution of the components in these systems, using the classical P—T—x phase diagrams. This interaction can result in the formation of solid solutions, segregations on the surface, and multiphase samples and in the stabilization of thermodynamically unstable phases. The phase composition, the chemical composition of the crystallite surface, the character of mutual distribution of the components, and the real structure of nanocomposites are specified by the conditions of synthesis. In turn, these properties determine the reactivity of the materials and the mechanism of their interaction with the gas phase, the concentration and mobility of charge carriers and, hence, the sensor characteristics, namely, the sensor signal value, selectivity, stability, and times of sensor response and relaxation.

In spite of various approaches to the directed choice of dopants for sensor materials using the electronegativity, electron affinity, thermodynamic parameters of adsorption, and a change in the electron work function[9,10] as

correlation parameters, the catalytic approaches based on the concepts of "collective" and "local" sites are most promising in our opinion. The consideration in the framework of the "collective" site approach is based on the theory of chemisorption on the semiconductor surface.[11] This theory describes the mechanism of the influence of an adsorbate on the common band structure of the modified matrix. The catalytic activity of the modifier is directly related to the valence state of doping impurities in the oxide matrix and their influence on the charge carrier concentration in the semiconductor. At the same time, the "local" site approach is based on the concepts on nonuniform surface. In this case, the interaction of a semiconducting oxide with the gas phase is described through the formation of surface complexes, and the decisive role in this process belongs to the chemical nature of the modifier and its reactivity in acid-base or redox reactions. The modifier for the creation of a selective sensitive material can preliminarily be chosen on the basis of an analysis of the properties of molecules of the gas to be detected and experimental data obtained in the field of heterogeneous catalysis on the Platinum Group metals and metal oxides[12−14] (Fig. 1). Obviously, the regularities found for catalysts can be invalid for sensor materials and should experimentally be checked.

In the present work, we review the results of our studies of a relationship between the composition, structure, chemistry of the surface, and sensor properties of the nanocomposites SnO$_2$—M$_n$O$_m$ (M$_n$O$_m$ = Fe$_2$O$_3$, MoO$_3$, V$_2$O$_5$).

1. Preparation of the materials and methods of investigation

Nanocrystalline SnO$_2$ and nanocomposites SnO$_2$—M$_n$O$_m$ (M$_n$O$_m$ = Fe$_2$O$_3$, MoO$_3$, V$_2$O$_5$) were prepared by various methods of chemical precipitation from solutions.[15−21]

The SnO$_2$-based nanocomposites were synthesized by the thermal decomposition of the α-stannic acid gel followed by impregnation with solutions of the corresponding metal salts. The α-stannic acid gel was precipitated[15−21] from an aqueous solution of SnCl$_4$·5H$_2$O by the addition of aqueous ammonia (to pH = 6.5—7.0) with continuous stirring at 0 °C. The precipitate was separated by centrifugation, thoroughly washed with distilled water to remove chloride ions until the negative reaction with AgNO$_3$ was achieved, and dried at 100 °C for 1 day. Then the powder was impregnated with aqueous solutions of Fe(NO$_3$)$_3$[18], (NH$_4$)$_6$Mo$_7$O$_{24}$,[19] or VO$_2$NO$_3$,[21] dried at 100 °C, and annealed in air at 300, 500, or 700 °C for 24 h. The M$_n$O$_m$-based nanocomposites were synthesized by the coprecipitation of α-stannic acid with the corresponding metal hydroxides followed by the thermal treatment.[18,19,21] Aqueous solutions of ammonia or hydrazine hydrate were used as precipitating reagents.

The nanocomposites synthesized were characterized by a complex of physicochemical methods to obtain information on the elemental and phase compositions, the distribution of components between the bulk and surface of crystalline grains, particle sizes, and the specific surface area.

The elemental composition of the nanocomposites was studied by electron-probe X-ray microanalysis (EPXMA). Quantitative analysis was performed on a Jeol 840A microscope with the PGT microanalytical system. Mechanical mixtures of oxides were used as reference samples. The analysis was performed at three windows (50×50 μm^2) using an accelerating voltage of 20 keV. The composition of the nanocomposites with respect to the metal cations was determined using the intensities of signals of Sn and the metal M (M = Fe, Mo, V) and the corresponding coefficients of the element sensitivity. Further the compo-
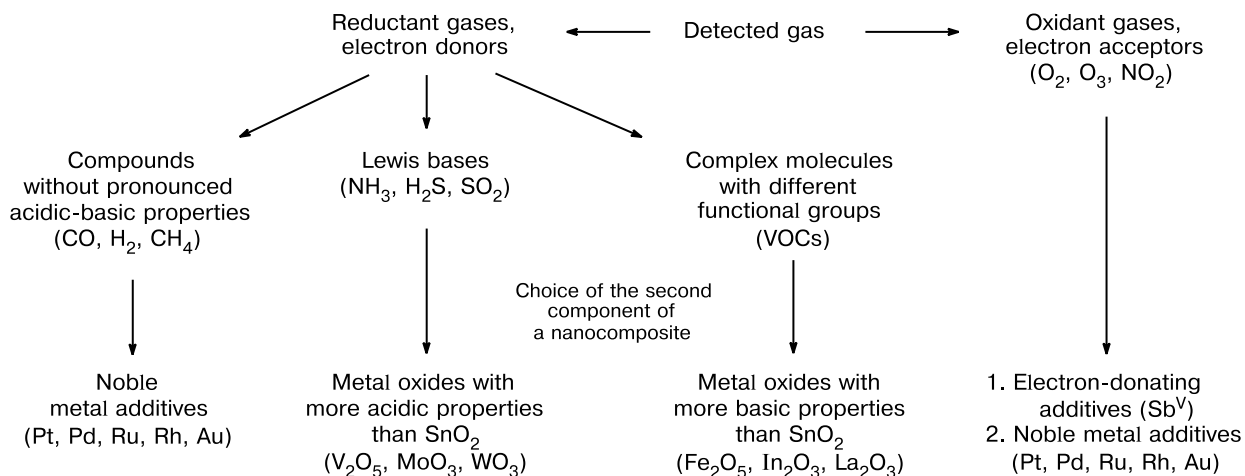

Fig. 1. Choice of the second component of the SnO$_2$-based nanocomposite with allowance for the properties of the detected gas.

sition of the samples is presented as atomic fractions (x) of the metal cations in the nanocomposite

$$x = [M]/([M] + [Sn]), \qquad (1)$$

where [M] and [Sn] are the concentrations (at.%) of M (M = Fe, Mo, V) and tin, respectively, determined from the EPXMA data.

The X-ray diffraction spectra of the nanocomposites were obtained on the Swiss—Norwegian line at the European Synchrotron Radiation Facility (ESRF, Grenoble) using the monochromatic radiation at $\lambda_{synchr} = 0.72004$ Å. The sizes of the coherent scattering regions (CSR) were estimated from the reflection broadening in the X-ray diffraction spectra by the Sherrer formula

$$d = k\lambda/(\beta\cos\theta), \qquad (2)$$

where d is the average size of the CSR, β is the diffraction peak width at the half-height, λ is the wavelength of the radiation used, θ is the diffraction angle, and $k = 0.9$.

The samples were studied by transmission electron microscopy and electron-probe X-ray microanalysis with a Phillips CM30 SuperTwin electron microscope (resolution 0.19 nm).

Mössbauer spectra were recorded on an electrodynamic type spectrometer in the permanent acceleration mode using the Ca^{119m}SnO$_3$ and ^{57}Co(Rh) sources, which were kept at room temperature. Isomeric shifts were measured relative to CaSnO$_3$ or α-Fe at 24 °C.

The acidic properties of the surface of the SnO$_2$—Fe$_2$O$_3$, SnO$_2$—V$_2$O$_5$, and SnO$_2$—MoO$_3$ nanocomposites were studied by temperature-programmed desorption of ammonia (NH$_3$-TPD). The experiments were carried out using an NH$_3$—N$_2$ (1 : 1) gas mixture. Before the analysis, the nanocomposites were degassed in a flow of helium for 2 h at 400 °C. Ammonia was adsorbed at room temperature. The NH$_3$-TPD experiments were carried out in helium flow after purging the sample at 50 °C during 60 min to remove the physically adsorbed ammonia. The temperature was increased to 800 °C at a rate of 8 °C min^{-1}. The number of acid sites (A) and the distribution with respect to the activation energy of ammonia desorption[22] was calculated assuming that one NH$_3$ molecule is desorbed from one acid site.

The oxidation properties of the nanocomponents were studied by temperature-programmed reduction with hydrogen (H$_2$-TPR) using an H$_2$—N$_2$ (5%) gas mixture. Before the analysis, the nanocomposited were degassed in a flow of helium for 2 h at 400 °C. The temperature was increased to 800 °C at a rate of 8 °C min^{-1}.

The sensor properties of the substances were studied depositing them as a paste on a microelectronic chip with platinum contacts and a platinum meander as a heater on the Al$_2$O$_3$ support. The conductivity was measured under dc conditions in the presence of a gas mixture containing 500 ppm NH$_3$ in air at $T = 400$ °C or upon the introduction of 1 μL of ethanol into the flow of air ($T = 275$ °C). The sensor signal value S was determined from the conductivity values in air G_0 and in the tested gas G by the formula

$$S = (G - G_0)/G_0. \qquad (3)$$

The catalytic activity of the SnO$_2$—Fe$_2$O$_3$ nanocomposites in ethanol oxidation was studied under an atmospheric pressure in a flow-type quartz microreactor. The powders were preliminarily pressed under a pressure of 50 MPa and crushed, and the fraction with a particle size of 0.5—1.0 mm was placed in the microreactor between the layers of quartz particles. The reactor was heated in the interval from 200 to 400 °C in a temperature-programmed tubular oven. Before the experiment, the nanocomposites were annealed for 6 h at 400 °C in a flow of dry air. Ethanol vapor was introduced into the reactor through a bubbler, whose temperature was maintained at 0 °C.

The ethanol oxidation products were identified by chromato-mass spectrometry on a Hewlett—Packard 5890 chromatograph with an HP-FFIP column and an HP 5971A detector. The amount of oxygen-containing products was determined using an M-3700 gas chromatograph with a Carbowax 6M column. The contents of light hydrocarbons, CO, and CO$_2$ were analyzed on a Chrom-5 chromatograph with Porapak-Q column (4 m).

2. Phase composition of the nanocomposites

An X-ray phase analysis of nanocomposites is a difficult task because of considerable broadening of nanocrystalline phase reflections. Therefore, additional methods are required.

The distribution of the modifier between the bulk and the surface of crystalline grains of the major phase is very important for the formation of functional properties of the nanocomposites. The insertion of admixture atoms into the crystalline structure of the semiconducting oxide results in the formation of impurity levels, the compensation effect of donor oxygen vacancies by acceptor admixture defects, and the modulation of the band relief of the semiconductor.[17] The segregation of the modifier can result in the formation of p—n-junctions in the region of intergrain contacts, which also inevitably affects the electrophysical properties of the material. In addition, the modifier distribution between the bulk and the surface of the crystalline grains determines its efficiency in the interaction between the material and gas phase. All these factors exert a considerable effect on the sensor properties of the nanocomposite.

The M$_n$O$_m$ oxide phase in nanocomposites is often observed only at high annealing temperatures and rather

large atomic fraction of the cation M, *i.e.*, of high values of x (see Eq. (1)). Similarly, the SnO$_2$ phase is not detected when the M$_n$O$_m$ oxide is the major phase. In these cases, a solid solution can be formed and/or the modificator can be segregated on the crystallite surface of the major phase. The contribution of this or another variant is determined by both fundamental factors, for example, the difference between the ion radii of Sn^{4+} (0.69 Å)[23] and M^{n+} and the conditions of synthesis, *viz.*, the chemical composition of the nanocomposite (x value) and annealing temperature. Taking into account the ion radii of the metal cations in the octahedral environment,[23] we can assume that SnO$_2$-based solid solutions are formed upon the introduction of Ni^{2+} (0.70 Å), Fe^{3+} (0.645 Å), and Mo^{4+} (0.65 Å). This is hardly probable in the case of Cu^{2+} (0.73 Å), Zn^{2+} (0.745 Å), La^{3+} (1.06 Å), Ce^{4+} (0.80 Å), and V^{5+} (0.54 Å).

A univocal conclusion about the formation of a solid solution can be made, if the crystal lattice parameters of the principal phase change with an increase in the x value. However, for the nanocrystalline systems it is often difficult to determine exactly the parameters from the X-ray diffraction data because of the already mentioned substantial reflection broadening in the diffraction patterns. Valuable additional information on the character of the mutual distribution of the components in the nanocomposites can be obtained by transmission electron microscopy, electron diffraction, Raman spectroscopy, and Mössbauer spectroscopy.

2.1. Nanocomposites SnO$_2$—Fe$_2$O$_3$. The X-ray diffraction data[18] (Table 1) show that in the SnO$_2$—Fe$_2$O$_3$ nanocomposites prepared by both the impregnation method (0 ≤ x ≤ 0.31) and hydroxide coprecipitation (0.18 ≤ x ≤ 1) the two-phase region corresponds to the

Table 1. Phase composition, average sizes of the coherent scattering regions (d_{XRD}(SnO$_2$)/nm, d_{XRD}(M$_n$O$_m$)/nm), and average particle size (d/nm) of the SnO$_2$—M$_n$O$_m$ nanocomposites (annealing at 500 °C)

x	Method[a]	X-ray diffraction			Electron microscopy, d
		Phase composition	d_{XRD}(SnO$_2$)	d_{XRD}(M$_n$O$_m$)	
		SnO$_2$—Fe$_2$O$_3$[b]			
0.00	—	SnO$_2$	9	—	9±1
0.03	I	SnO$_2$	7	—	6.2±0.6
0.08	I	SnO$_2$	6	—	4.4±0.6
0.13	I	SnO$_2$	5	—	5.5±0.7
0.31	II	SnO$_2$	4	—	3.4±0.3
0.37	II	SnO$_2$ + Fe$_2$O$_3$ + Fe$_{3-y}$Sn$_y$O$_{4+\delta}$	<3	<3	4.3±0.7
0.52	II	SnO$_2$ + Fe$_2$O$_3$ + Fe$_{3-y}$Sn$_y$O$_{4+\delta}$	<3	8	8±5
0.69	II	Fe$_2$O$_3$	—	11	14±3
0.85	II	Fe$_2$O$_3$	—	10	33±7
1.00	—	Fe$_2$O$_3$	—	24	35±8
		SnO$_2$—V$_2$O$_5$[c]			
0.00		SnO$_2$	6	—	<10
0.27	I	SnO$_2$	4	—	<10
0.52	II	SnO$_2$ + V$_2$O$_5$	6	25	50—100
0.73	II	SnO$_2$ + V$_2$O$_5$	7	29	100—300
0.90	II	SnO$_2$ + V$_2$O$_5$	6	30	100—300
1.00	—	V$_2$O$_5$	—	35	200—400
		SnO$_2$—MoO$_3$[b]			
0.00	—	SnO$_2$	10	—	8±1
0.04	I	SnO$_2$	8	—	5.0±0.5
0.06	I	SnO$_2$	6	—	2.4±0.4
0.17	I	SnO$_2$	4	—	2.6±0.6
0.22	I	SnO$_2$ + MoO$_3$	3	25	>100
0.40	I	SnO$_2$ + MoO$_3$	<3	23	>100
0.50	I	SnO$_2$ + MoO$_3$	<3	25	>100
0.70	I	SnO$_2$ + MoO$_3$	<3	25	>100
1.00	—	MoO$_3$	—	30	>100

[a] Methods of synthesis of the nanocomposites: I is impregnation, and II is coprecipitation of hydroxides.
[b] The average particle size d was determined from the data of transmission electron microscopy.
[c] The average particle size d was determined from the data of scanning electron microscopy.

tervals $0.37 \leq x \leq 0.52$ at $T = 300$ and $500\,°C$ or $0.31 \leq x \leq 0.85$ at $T = 700\,°C$. The diffraction patterns of the nanocomposites with $x = 0.37$ and 0.52 annealed at 300 and 500 °C (Fig. 2) indicate the formation of Fe_3O_4-based solid solutions with the spinel structure.[24] The change in the position of the most intense reflection (311) of $Fe_{3-y}Sn_yO_{4+\delta}$ indicates an increase in the tin concentration in the solid solution with an increase in both the SnO_2 content in the nanocomposite and the annealing temperature. The partial reduction of iron in these samples is due to the use of hydrazine hydrate as the precipitating agent in the synthesis by hydroxide coprecipitation.

The quantitative phase composition of the nanocomposites annealed at 700 °C was estimated by the Chung method using the reference intensity ratio (RIR) — the ratio of absolute intensities of the strongest reflections of a given substance and corundum (α-Al_2O_3) in the diffraction pattern of a mixture containing 50 wt.% of each

component).[25] The component mass fraction X_α was calculated by the formula

$$X_\alpha = \frac{I_{i\alpha}}{RIR_\alpha \cdot I_{i\alpha}^{rel}} \left(\sum_{k=1}^{n} \frac{I_{jk}}{RIR_k \cdot I_{jk}^{rel}} \right)^{-1}, \tag{4}$$

where $I_{i\alpha}$ is the measured absolute intensity for the ith reflection of the component α in the diffraction pattern, $I_{i\alpha}^{rel}$ is the relative intensity of this reflection in the PDF-2 base, RIR_α is the reference intensity ratio for the determined phase ($RIR_{SnO_2} = 1.9$, $RIR_{\alpha\text{-}Fe_2O_3} = 2.4$), and I_{jk}, I_{jk}^{rel}, and RIR_k are the corresponding values for all (including α) components of the mixture. The most intense reflections of Fe_2O_3 (104) ($d = 2.6999$ Å), (110) ($d = 2.5190$ Å) and SnO_2 (110) ($d = 3.3471$ Å), (101) ($d = 2.6427$ Å) were used for the analysis. The results are shown in Fig. 3 where the molar fraction of the α-Fe_2O_3 phase ($\nu_{\alpha\text{-}Fe_2O_3}$) determined by the Chung method from the diffraction data is compared with an analogous value calculated from the EPXMA results assuming that all Sn atoms are localized in the SnO_2 phase and all Fe atoms are in the α-Fe_2O_3 phase

$$\nu_{\alpha\text{-}Fe_2O_3} = 2x/(2 - x), \tag{5}$$

where

$$x = [Fe]/([Fe] + [Sn]).$$

In the absence of the interaction between the nanocomposite components (for instance, in the case of mechanical mixtures of powders of the corresponding oxides), the amount of each phase should correspond to the dashed line in Fig. 3. According to the obtained experimental results (points in Fig. 3), a portion of Fe_2O_3 (or, correspondingly, SnO_2) forms a solid solution or a segregation[26] on the surface of crystalline grains of the main component.
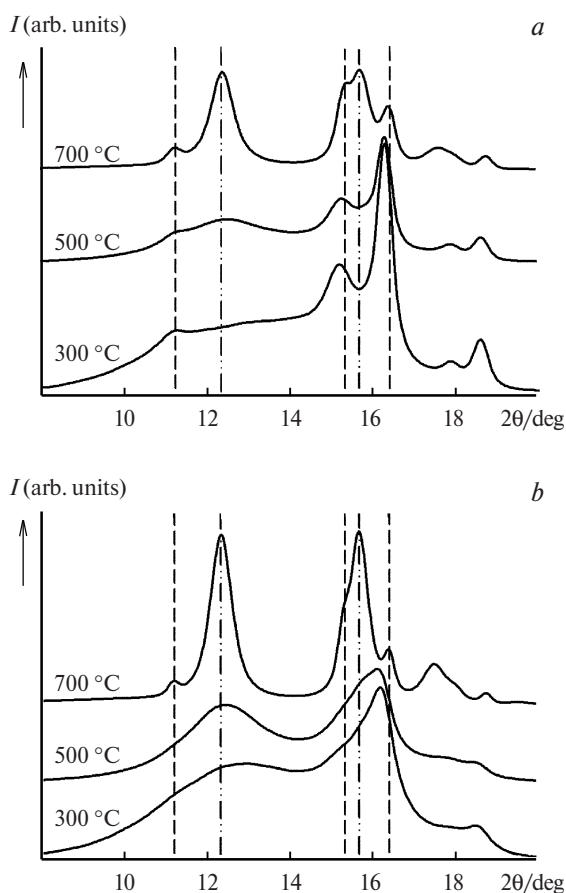

Fig. 2. Diffraction patterns of the SnO_2—Fe_2O_3 nanocomposites with $x = 0.37$ (*a*) and 0.52 (*b*) annealed at different temperatures. The lines mark the positions of the most intense reflections of Fe_2O_3 (dashed lines) (104) ($d = 2.6999$ Å) and (110) ($d = 2.5190$ Å) and SnO_2 (dash-and-dot lines) (110) ($d = 3.3471$ Å) and (101) ($d = 2.6427$ Å).
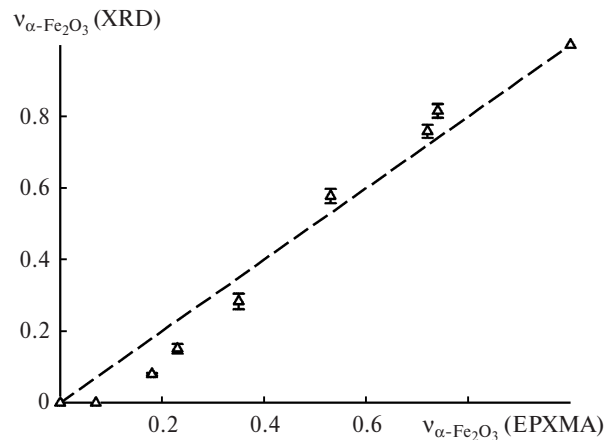

Fig. 3. Quantitative phase analysis of the SnO_2—Fe_2O_3 nanocomposites annealed at 700 °C: a comparison of the molar fractions of the α-Fe_2O_3 phase determined from the diffraction data and calculated from the EPXMA results.

The changes in the unit cell parameters *a* and *c* of SnO₂ and Fe₂O₃ were observed for the nanocomposites in which the phase of the second component is not detected, which suggests the formation of solid solutions based on both cassiterite and hematite (Fig. 4). In all cases, the change in the crystalline lattice parameters is determined by two factors: the elemental composition of the nanocomposite and the annealing temperature. The unit cell parameters of pure SnO₂ remain almost unchanged with an increase in the annealing temperature, which suggests that the observed dependences of $a(x)$ and $c(x)$ are related to the formation of solid solutions based on the cassiterite structure in the SnO₂—Fe₂O₃ system rather than to the change in the degree of crystallinity of the phase. The unit cell parameter *a* of SnO₂ (see Fig. 4) decreases in the composition range $0 \leq x \leq 0.31$, and the slope of the $a(x)$ plot changes at $x = 0.09$ regardless of the annealing temperature. Analogous tendencies are also characteristic of the *c* parameter of the SnO₂ unit cell. This indicates the change in the character of the Fe distribution between the crystalline lattice (grain bulk) and the surface of the SnO₂ crystallites. The data presented in Fig. 4, *a* indicate that
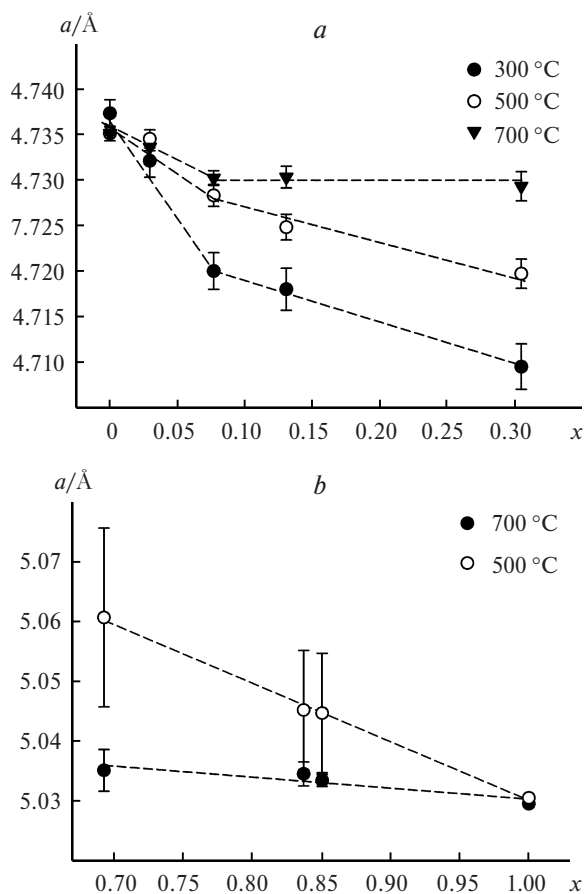
the solubility of Fe in SnO₂ decreases with an increase in the annealing temperature.

The unit cell parameters *a* (see Fig. 4, *b*) and *c* of α-Fe₂O₃ increase with an increase in the Sn content in the nanocomposites. These changes seem to be more considerable at lower annealing temperatures (300 and 500 °C). However, the error in estimation of this parameter is also maximum in this case. In all cases, the direction of changes in the unit cell parameters is consistent with the ratio of the ion radii of Sn⁴⁺ (0.69 Å) and Fe³⁺ (0.645 Å). The content of the second component in the solid solution (iron in SnO₂ and tin in Fe₂O₃) cannot be determined by the EPXMA method due to small particle sizes in the nanocrystalline systems. The Fe^III and Sn^IV concentrations in the SnO₂- and Fe₂O₃-based solid solutions were estimated from the changes in the unit cell volumes of SnO₂ and Fe₂O₃, respectively, using the Vegard law and suggest that the solubility of Fe^III in SnO₂ and Sn^IV in Fe₂O₃ is lower than the total content of the corresponding metal determined by the EPXMA method (Fig. 5). A portion of the second component not involved in the solid solution can form crystallites of its own phase or segregate on the grain surface of the major phase as a two-dimensional layer, which is not detected by X-ray diffraction. Owing to the difference in the crystal structures of SnO₂ and α-Fe₂O₃ and the necessity for charge compensation in heterovalent substitution, the extension of the solid solution region cannot be considerable. Higher imperfection of the matrix in the nanocomposites annealed at low temperatures ensures higher solubility of the second component. The decrease in the solubility of Fe^III in SnO₂ and Sn^IV in Fe₂O₃ with the temperature increase has been shown previously[27,28] by EXAFS and Mössbauer spectroscopy.

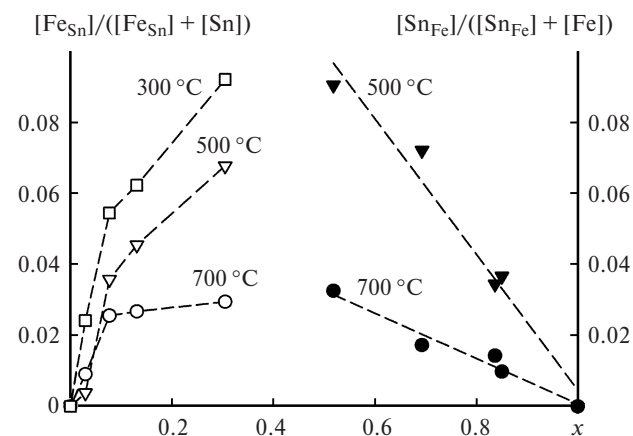Additional information on the mutual distribution of the components in the SnO₂—Fe₂O₃ nanocomposites

Fig. 4. Unit cell parameter *a* for SnO₂ (*a*) and Fe₂O₃ (*b*) in the SnO₂—Fe₂O₃ nanocomposites with various composition, $x = $ [Fe]/([Fe] + [Sn]).

Fig. 5. Estimation of the Fe^III concentration in SnO₂ ([Fe_Sn]/([Fe_Sn] + [Sn])) (light symbols) and Sn^IV in Fe₂O₃ ([Sn_Fe]/([Sn_Fe] + [Fe])) (dark symbols) on the basis of a change in the unit cell volume of SnO₂ and Fe₂O₃ using the Vegard law, $x = $ [Fe]/([Fe] + [Sn]).

($0 \leq x \leq 0.13$) synthesized by impregnation was obtained by Raman spectroscopy. The bands of the α-Fe$_2$O$_3$ phase appear at the iron content $x > 0.1$. The position of the main band A$_{1g}$ of SnO$_2$ shifts to smaller wave numbers with an increase in x, which confirms the formation of the SnO$_2$-based solid solution (Fig. 6).

Another informative parameter is the ratio I_r

$$I_r = I_S/I_{A_{1g}}, \qquad (6)$$

where I_S is the total intensity of the surface modes of nanocrystalline SnO$_2$, and $I_{A_{1g}}$ is the integral intensity of the A$_{1g}$ line in the Raman spectrum.[29] This parameter was used earlier[30] to illustrate that the CuO monolayer can be formed on the SnO$_2$ grain surface in SnO$_2$—CuO composites. In the SnO$_2$—Fe$_2$O$_3$ system, the increase in I_r with an increase in x suggests the absence of a specific interaction between SnO$_2$ and α-Fe$_2$O$_3$ on the crystallite surface. Thus, the Fe atoms not involved in the solid solution do not segregate in the form of a Fe$_2$O$_3$ monolayer as in the case of SnO$_2$—CuO, but form three-dimensional α-Fe$_2$O$_3$ particles, which are detected only by Raman spectroscopy due to a higher sensitivity of this method to the Fe$_2$O$_3$ phase as compared to X-ray diffraction.

The Raman spectra of a series of samples prepared by the decomposition of coprecipitated tin and iron hydroxides exhibit the bands of α-Fe$_2$O$_3$ at the iron oxide content $x \geq 0.31$. An analysis of the characteristic features of the Raman spectra, namely, the positions of the maximum (Fig. 7) and width of the most intense line of hematite (E$_g$), demonstrates differences in the component distribution associated with the method of synthesis. The parameters of the E$_g$ line of Fe$_2$O$_3$ in the spectra of the nanocomposites prepared by the impregnation method are close to the values corresponding to the α-Fe$_2$O$_3$ phase. To the contrary, in the Raman spectra of the sam-

ples synthesized by coprecipitation followed by hydroxide decomposition, the wave number corresponding to the position of the E$_g$ maximum of Fe$_2$O$_3$ increases strongly and the linewidth decreases monotonically with an increase in x. This change in the spectra indicates the formation of crystallites of the α-Fe$_2$O$_3$ phase in the synthesis by impregnation and formation of a solid solution based on α-Fe$_2$O$_3$ for the synthesis by coprecipitation. In the former case, the precursor Fe(NO$_3$)$_3$ is distributed over the surface of the dispersed matrix of the dried α-stannic acid gel, and in the thermal treatment and with exceeding solubility of Fe^{III} in the cassiterite structure, an excess of this component crystallizes as an independent oxide phase. Hydroxide coprecipitation results in the formation of a precursor in which the Sn and Fe atoms are located at short distances from each other, which allows formation of solid solutions on the basis of both cassiterite and hematite.

The most detailed information on the mutual component distribution in the nanocrystalline system SnO$_2$—Fe$_2$O$_3$ can be obtained by Mössbauer spectroscopy. In this case, studies can be carried out using two Mössbauer isotopes, $viz.$, ^{57}Fe and ^{119}Sn. An additional advantage of Mössbauer spectroscopy for studying the SnO$_2$—Fe$_2$O$_3$ system is related to the spin polarization of the nonmagnetic tin ions induced by the adjacent 3d-cations, leading to the appearance of the magnetic hyperfine splitting[31] in the ^{119}Sn spectra. The latter provides information on the tin distribution relative to the magnetically ordered α-Fe$_2$O$_3$ crystallites. The parameters of magnetic hyperfine splitting of ^{119}Sn have been determined[31—33] for the first time by studying the samples containing small amounts of the Sn^{4+} ions (≤ 0.5 at.%) in the bulk of the crystalline α-Fe$_2$O$_3$ particles. The Sn^{4+} ions occupy positions of the same type and
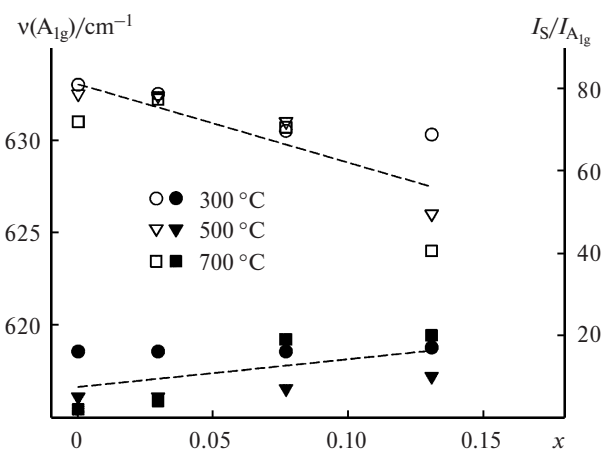

Fig. 6. Characteristics of the Raman spectra of the SnO$_2$—Fe$_2$O$_3$ nanocomposites annealed at different temperatures: the position of the maximum of the A$_{1g}$ SnO$_2$ line (open symbols) and $I_S/I_{A_{1g}}$ ratio (closed symbols), $x = $ [Fe]/([Fe] + [Sn]).
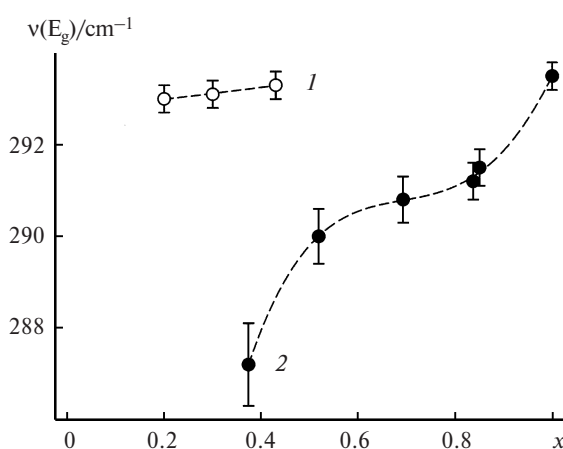

Fig. 7. Position of the maximum of the E$_g$ Fe$_2$O$_3$ line in the Raman spectra of the SnO$_2$—Fe$_2$O$_3$ nanocomposites prepared by the impregnation (*1*) and coprecipitation (*2*) method, $x = $ [Fe]/([Fe] + [Sn]).

at 295 K are characterized by the magnetic hyperfine field $H(Sn) = 123$ kOe and isomeric shift $\delta = +0.15$ mm s^{-1}. Thus, these parameters made it possible to identify the Sn^{4+} ions in the structure of the matrix under study. It was found[31] that the maximum content of Sn^{4+} in $\alpha\text{-}Fe_2O_3$ did not exceed 1 at.% for the samples prepared by coprecipitation of tin and iron hydroxides followed by annealing at 900 °C. Subsequent studies of the system (Sn : Fe = 1 : 1) prepared by an analogous method showed[34] that the $\alpha\text{-}Fe_2O_3$ crystallites manifested the superparamagnetic properties, which suggests their small sizes ($d < 14$ nm).[35]

The ^{119}Sn spectra of the $SnO_2\text{—}Fe_2O_3$ samples with a small iron content ($x \leq 0.09$) represent singlets with the parameters corresponding to pure SnO_2. The ^{57}Fe spectra (24 °C) of these samples contain no magnetic HFS and exhibit quadrupole doublets with $\delta \sim 0.3$ mm s^{-1} and $\Delta \sim 1$ mm s^{-1}. The ^{57}Fe parameters indicate the uniform distribution of iron oxide in the SnO_2 sample without the formation of $\alpha\text{-}Fe_2O_3$ clusters, whose diameter is larger than 10 nm, which confirms the formation of a cassiterite-based solid solution.

Studies of nanocomposites with high iron content ($0.84 \leq x \leq 1$) made it possible to estimate the solubility of Sn^{IV} in hematite. The ^{119}Sn spectrum (-193 °C) of the nanocomposite with $x = 0.84$ (Fig. 8) revealed an unexpectedly high content of the Sn^{4+} cations subjected to spin polarization. This indicates that in the sample studied a considerable fraction ($>2/3$) of tin atoms has iron cations in the local environment. Annealing at 900 °C results in the decomposition of this structure and isolation
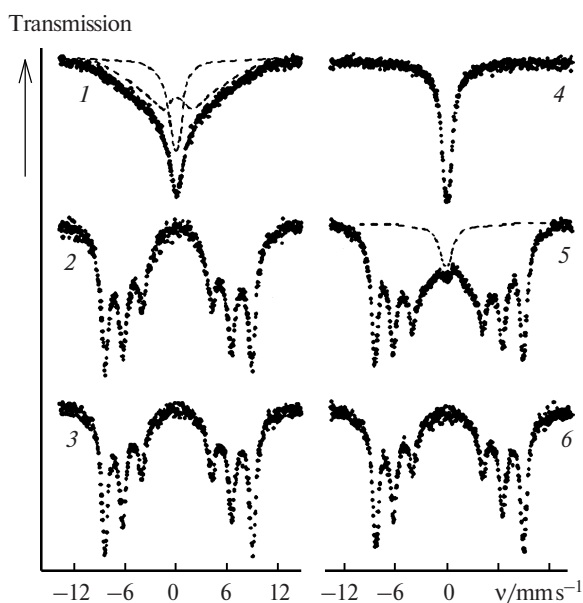
of the SnO_2 phase. An analogous process is observed (to a considerably lesser extent) for the $SnO_2\text{—}Fe_2O_3$ nanocomposite ($x = 0.995$): small contribution of the nonmagnetic component appears additionally in the center of the spectrum after annealing at 900 °C. No SnO_2 segregations are observed upon annealing of the nanocomposite with the minimum tin content ($x = 0.998$). The parameters of the ^{119}Sn spectrum remain unchanged with an increase in the annealing temperature to 900 °C and correspond to the values obtained earlier[31,33,36—39] for the solid solution of Sn^{IV} substitution in $\alpha\text{-}Fe_2O_3$. Thus, the effective solubility of Sn^{IV} in hematite decreases with an increase in the annealing temperature and at 900 °C it does not exceed 0.3—0.4 at.% Sn.

The ^{57}Fe spectra (24 °C) of the nanocomposite ($x = 0.84$) annealed at 300 and 500 °C (Fig. 9) represent[27] the superposition of the sextet with the parameters corresponding to $\alpha\text{-}Fe_2O_3$ and the central doublet that can be attributed to fine (superparamagnetic) $\alpha\text{-}Fe_2O_3$ particles with a diameter smaller than 14 nm.[35] The ^{57}Fe spectra obtained at -193 °C exhibit only the sextet of the magnetic HFS with the parameters $\delta = 0.48\pm0.05$ mm s^{-1} and $H = 525\pm10$ kOe, which suggests that the samples contain no $\alpha\text{-}Fe_2O_3$ crystallites with the sizes smaller than 8 nm.[35] The ^{57}Fe spectrum (24 °C) of the $SnO_2\text{—}Fe_2O_3$ nanocomposite ($x = 0.84$) annealed at 700 °C contains

Fig. 8. ^{119}Sn Mössbauer spectra of the $SnO_2\text{—}Fe_2O_3$ nanocomposites annealed at 500 (*1—3*) and 900 °C (*4—6*) with $x = 0.84$ (*1, 4*), 0.995 (*2, 5*), and 0.998 (*3, 6*) detected at -193 (*1, 4*) and 24 °C (*2, 3, 5, 6*).
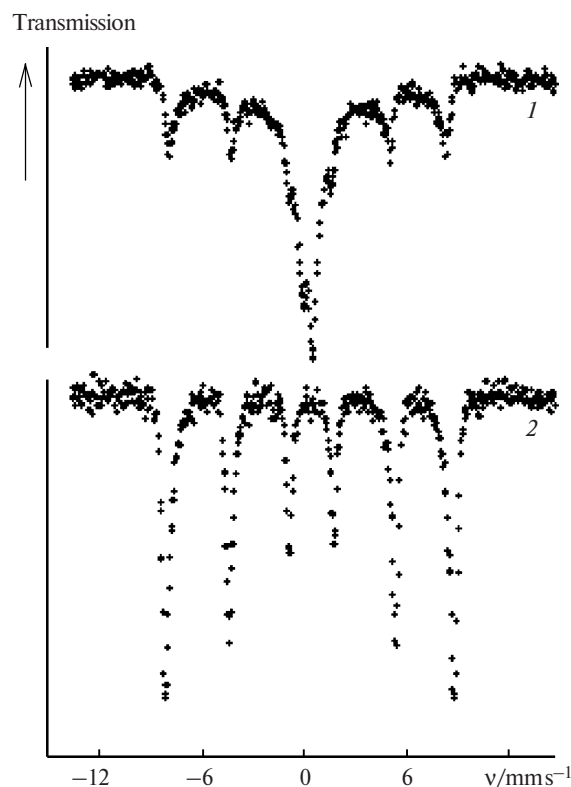

Fig. 9. ^{57}Fe Mössbauer spectra of the $SnO_2\text{—}Fe_2O_3$ nanocomposite ($x = 0.84$, annealing at 500 °C) detected at 80 (*1*) and 297 K (*2*).

only the magnetic HFS indicating crystallization of the supermagnetic α-Fe_2O_3 particles with the diameter 8 nm $< d <$ 14 nm.

A comparison of the data obtained using the ^{57}Fe and ^{119}Sn probing ions at -193 °C suggests that ~2/3 of Sn atoms are spin-polarized and the remaining 1/3 Sn exists as nonmagnetic clusters of the SnO_2 type, whereas all the iron atoms exist in the magnetically ordered state. This unambiguously indicates the partial segregation of tin around the finest α-Fe_2O_3 crystallites. In fact, the higher specific surface of the particles covered with tin (8 nm $< d <$ 14 nm) makes it possible to explain the presence of many spin-polarized Sn^{4+} ions, whose concentration considerably exceeds the maximum tin concentration in the bulk of the crystallite. In addition, the occupation with tin of positions with the nonequivalent cationic (magnetically active) environment, which are present on the surface of the α-Fe_2O_3 crystallites, explains the absence of the resolved structure in the magnetically split component.

It can be assumed that various exchange bonds Fe^{3+}—O—Sn^{4+} were formed due to the decomposition of the corresponding hydroxides. The formation of the tin segregation on the surface of the α-Fe_2O_3 crystallites should prevent their further growth. Annealing at 700 °C results in the complete decomposition of the exchange Fe^{3+}—O—Sn^{4+} bonds. This effect agrees with the low solubility of Sn^{4+} in the α-Fe_2O_3 bulk resulting in fast saturation of the near-surface layer and isolation of the SnO_2 clusters with further enlargement of the finest crystallites.

2.2. Nanocomposites SnO_2—V_2O_5. In the SnO_2—V_2O_5 nanocomposites, the two-phase region at $T = 500$ °C corresponds[21] to the composition interval $0.27 < x \leq 0.90$ (see Table 1). In the single-phase region at $0 < x \leq 0.27$, the unit cell parameters of SnO_2 decrease, which is related, most likely, to the formation of a solid solution of V^{IV} in tin dioxide (the ion radius of Sn^{4+} is 0.69 Å, and that of V^{4+} is 0.63 Å). The content of V^{IV} in the SnO_2-based solid solution estimated from the decrease in the cell volume according to the Vegard law is $[V_{Sn}]/([V_{Sn}] + [Sn]) \leq 0.01$. No changes in the unit cell parameters of V_2O_5 are observed in the region $0.90 \leq x < 1$, which is due to the low solubility of Sn^{IV} in V_2O_5 because of the high difference in the ion radii of Sn^{4+} and V^{5+}.

The Raman spectra are very sensitive[21] to the presence of the V_2O_5 crystalline phase in the samples. Since the Raman spectra of the SnO_2—V_2O_5 nanocomposites with $0 < x \leq 0.27$ contain no bands of crystalline V_2O_5, it can be assumed that vanadium, which did not enter the SnO_2-based solid solution, forms in these nanocomposites an amorphous phase uniformly distributed over the grain surface of tin dioxide.

Additional information on the mutual component distribution in the SnO_2—V_2O_5 nanocomposites ($0.5 \leq x \leq 1$)

was obtained by scanning electron microscopy in the chemical contrast mode. The experiment was carried out on a LEO S440 instrument. The microphotograph of the SnO_2—V_2O_5 nanocomposite ($x = 0.90$) is shown in Fig. 10. The sample contains irregular particles with the sizes from 30 to 300 nm. Rare lighter areas smaller than 10 nm in size are observed against the uniform background in the chemical contrast mode. This indicates that tin is present in the nanocomposite as particular SnO_2 nanocrystallites on the grain surface of the V_2O_5 phase.

2.3. Nanocomposites SnO_2—MoO_3. According to the X-ray diffraction data, the two-phase region in the SnO_2—MoO_3 nanocomposites at $T = 500$ °C corresponds[19,40] to the interval $0.22 \leq x \leq 0.70$ (see Table 1). The strongly broadened reflections of the tin dioxide phase and the superposition of the lines corresponding to SnO_2 and MoO_3 do not allow us to calculate the crystal lattice parameters with an accuracy sufficient to conclude about the existence of solid solutions.

The changes in the interplanar distances in the tin dioxide structure and small changes in the unit cell parameter of SnO_2, which increase with an increase in x, were found[40] in the nanocomposites with a low Mo content ($x \leq 0.1$) by high-resolution transmission microscopy. This indicates that Mo is present in the SnO_2 crystal structure and a solid solution is formed. The SnO_2 crystal structure is stabilized with further increase in x ($x > 0.1$). When $x = 0.04$ is achieved, the β-MoO_3 phase with the monoclinic structure is formed as a segregation of the tin dioxide particles on the surface. This segregation is not detected by X-ray diffraction. At $x > 0.17$ an orthorhombic α-MoO_3 phase is formed as large particles (>100 nm), whose surface contains small (3 nm) SnO_2 particles (Fig. 11, see Table 1).

The formation of the β-MoO_3 phase with the monoclinic structure was also proved by Raman spectroscopy (Fig. 12). The lines corresponding to β-MoO_3 appear in the Raman spectra of the SnO_2—MoO_3 nanocomposites
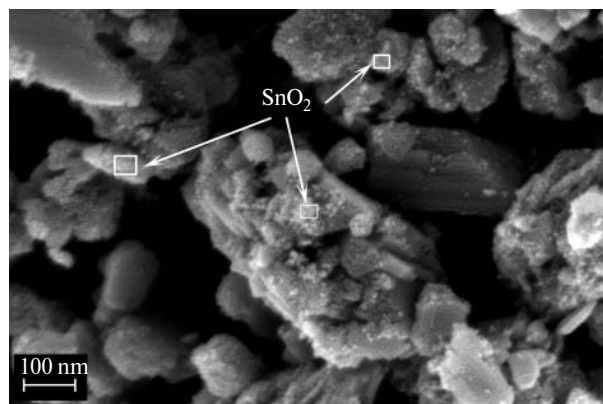

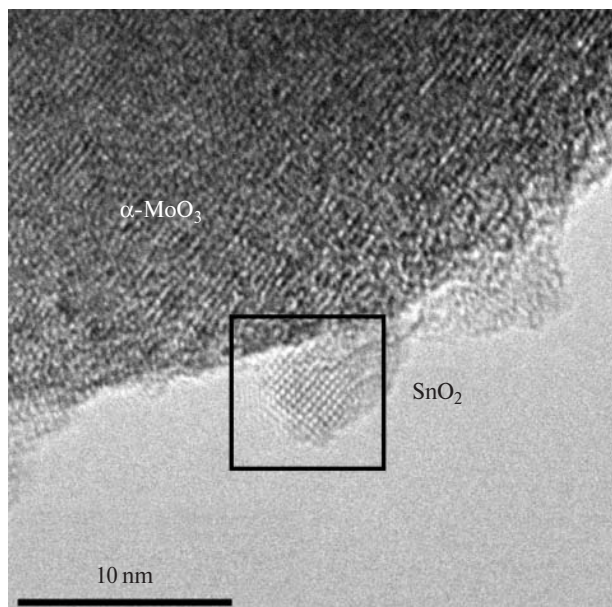**Fig. 10.** Microphotograph of the SnO_2—V_2O_5 nanocomposite ($x = 0.90$).

Fig. 11. Microphotograph of the SnO$_2$—MoO$_3$ nanocomposite ($x = 0.60$) obtained by high-resolution transmission electron microscopy.

in the range $0.04 \le x \le 0.17$. The intensity of the A$_{1g}$ line of SnO$_2$ (634 cm^{-1}) decreases simultaneously. The signal from α-MoO$_3$ appears at $x = 0.17$. The increase in the molybdenum content to $x = 0.27$ results in complete disappearance of the lines corresponding to β-MoO$_3$. The presence of the β-MoO$_3$ phase in the nanocomposites annealed at 500 °C is unexpected, because the phase transition β-MoO$_3 \rightarrow$ α-MoO$_3$ in the bulk samples occurs[41] at $T < 400$ °C. Probably, the β-MoO$_3$ phase is stabilized on the surface of small (~3 nm) tin dioxide particles (see Table 1).

The study of the mutual component distribution in the SnO$_2$—MoO$_3$ nanocomposites was supplemented by fine structure analysis in electron energy loss near-edge spectra (O K-edge ELNES).[40] The analysis was performed separately for the SnO$_2$ and MoO$_3$ crystallites (Fig. 13). The spectrum of SnO$_2$ contains two lines S$_1$ and S$_2$ at 535 and 542 eV, respectively. The same region of the spectrum of the MoO$_3$ particles also exhibits two lines: the main peak M$_1$ (535 eV) with the pronounced shoulder M$_2$ (538 eV). The spectrum of the SnO$_2$ particles is determined by the electronic levels of oxygen O2p or hybridized orbitals O2p—Sn5p and corresponds to the tetrahedral environment in the first coordination sphere of oxygen in the cassiterite structure.[42,43] The spectrum of the MoO$_3$ particles is determined by the hybridized orbitals O2p—Mo4d and corresponds to the octahedral environment of molybdenum with orbital splitting in the crystalline field to the t$_{2g}$ (M$_1$) and e$_g$ (M$_2$) levels.[44]

The analysis of the ratio of the S$_1$ and S$_2$ peak intensities (I_{S_1}/I_{S_2}) (Fig. 14) made it possible to refine the mo-
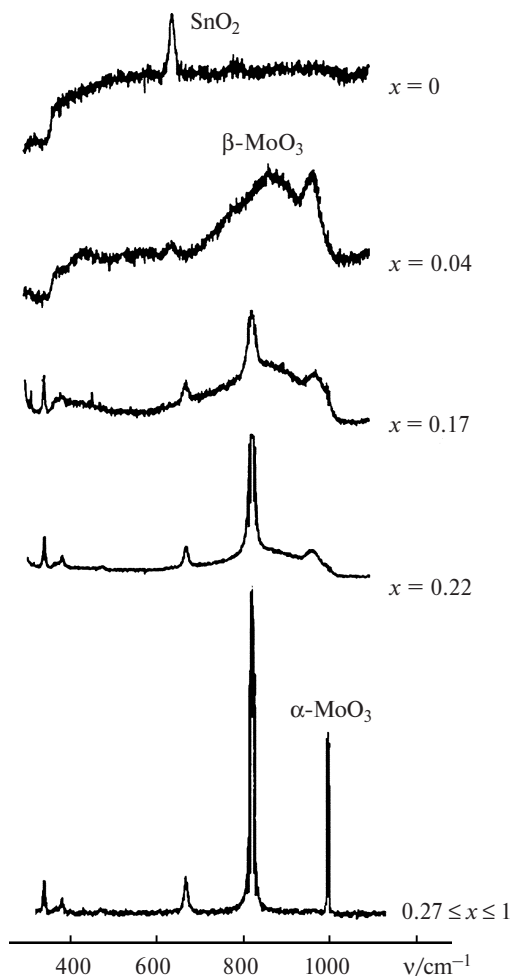

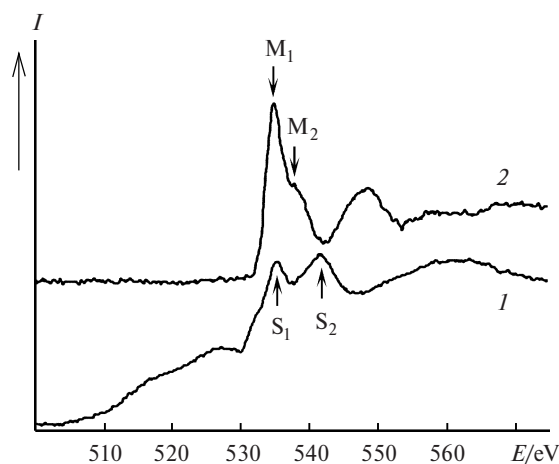**Fig. 12.** Raman spectra of the SnO$_2$—MoO$_3$ nanocomposites.

Fig. 13. Electron energy loss near-edge spectra (O K-edge ELNES) of the SnO$_2$ and MoO$_3$ particles.

lybdenum distribution in the SnO$_2$—MoO$_3$ nanocomposites. Three different regions were revealed in the plot of I_{S_1}/I_{S_2} vs molybdenum content. A smooth increase in $I_{S_1}/$
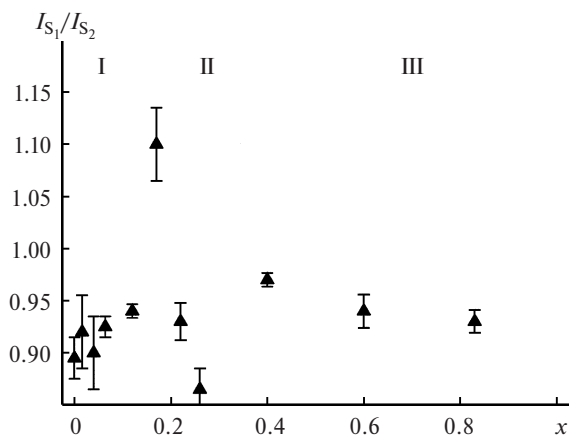
Fig. 14. Intensity ratios of the S_1 and S_2 peaks in the electron energy loss near-edge spectra (O K-edge ELNES) of the SnO_2—MoO_3 nanocomposites, $x = [Mo]/([Mo] + [Sn])$.

I_{S_2} due to an increase in the intensity of S_1 (535 eV) is observed in region I corresponding to $0 \leq x \leq 0.12$. This is due to an increase in the molybdenum content in the SnO_2 particles, because the M_1 peak (535 eV) coincides with S_1 and increases its integral intensity as compared to S_2. However, since the β-MoO_3 phase is detected by Raman spectroscopy at $x \geq 0.04$, it should be assumed that the solubility of Mo^{VI} in the cassiterite structure is low and the most part of Mo exists on the SnO_2 crystallite surface as a β-MoO_3 segregation.

Region III corresponds to the interval $0.40 \leq x \leq 0.83$. In this region, the I_{S1}/I_{S2} value slightly decreases with an increase in x. This suggests that the surface of the tin dioxide particles was saturated with molybdenum. The main portion of Mo is present in the nanocomposites as large α-MoO_3 particles.

Transition region II ($0.17 \leq x \leq 0.26$) exhibits large scatter of the data obtained by the analysis of various nanoparticles, indicating the molybdenum distribution between β-MoO_3 and α-MoO_3. This agrees well with the results obtained by Raman spectroscopy and electron diffraction.

2.4. Main regularities. An analysis of the experimental data altogether makes it possible to reveal the following main regularities.

1. The method of synthesis affects the modifier distribution between the bulk and surface of crystalline grains of the major phase. The introduction of the second component (modifier) by impregnation results in its concentration on the crystallite surface of the major phase. Since diffusion in the solid phase is slow, kinetic hindrance do not allow the second component to incorporate completely into the crystalline structure of the major phase. This is an additional factor facilitating the crystallization of the second component in the form of the own oxide phase. The use of the coprecipitation method provides a high degree of homogenization of the compo-

nents, short diffusion routes and, hence, a possibility to form solid solutions.

2. An increase in the content of the second component results in the successive formation of a solid solution based on the component present in a higher concentration, the segregation of the second component oxide as a monolayer or islets on the crystallite surface of the major phase, and then the transition to the two-phase region (Fig. 15).

3. The positions of the boundaries x_1, x_2, x_3, and x_4 (see Fig. 15) are determined by the ratio of ion radii of M^{n+} and Sn^{4+} and imperfection of the SnO_2 structure. The extension of the solid solution regions are equal to units of percents. The positions of the x_1 and x_4 boundaries are conventional, because the distribution coefficient of the second component between the solid solution and surface segregation cannot be determined precisely. The imperfection of the SnO_2 structure and the solubility of the second component decrease with an increase in the annealing temperature.

4. The high surface energy of the SnO_2 particles with ~3 nm in size in the SnO_2—MoO_3 nanocomposites leads to the stabilization of the thermodynamically metastable β-MoO_3 phase in the form of surface segregation.

3. Particle sizes and specific surface area

The sensor signal value and catalytic activity of the nanocrystalline oxides correlate with the specific surface area accessible for adsorption.[45] The specific surface area can usually be increased by decreasing the particle size. However, sensor measurements for a prolonged time at elevated temperatures (100—500 °C) induce the growth and aggregation of the particles and, therefore, decrease the stability of the properties of the sensor element.

The thermal stability in nanocrystalline materials can be increased by the modification of the crystalline grain boundaries by introducing the second component[46] or replacing the surface hydroxy groups by other functional groups that prevent polycondensation processes and particle aggregation.[47] The introduction of the second com-
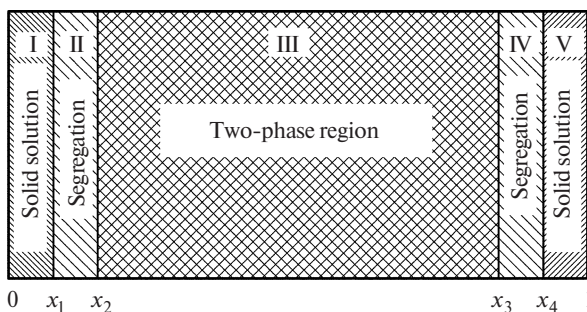

Fig. 15. Scheme of the mutual distribution of the components in the SnO_2—M_nO_m nanocomposites, $x = [M]/([M] + [Sn])$.

ponent decreases the total free energy of the boundaries at sites of the contact of different phases and decreases the total surface of contact between intrinsic crystallites of each ultradispersed phase. As a result, the rate of crystalline grain growth decreases considerably.

According to the data of transmission electron microscopy, the introduction of the second component into the SnO_2—Fe_2O_3 nanocomposites induces[18] a decrease in the particle size for both SnO_2 and Fe_2O_3 (Fig. 16). The average sizes of the coherent scattering regions (CSR) of SnO_2 and α-Fe_2O_3 (see Table 1) estimated by the Sherrer formula (2) suggest that an increase in the amount of the second component decreases the CSR sizes of the major phase at all annealing temperatures. The CSR values of the main component phase ($d_{XRD}(SnO_2)$, $d_{XRD}(Fe_2O_3)$) and the average particle size determined by transmission electron microscopy (d_{TEM}) are compared

in Fig. 17. Satisfactory agreement between the obtained data indicates that it is due to the small size of the CSR the reflection broadening in the X-ray diffraction pattern is observed and can be used for the estimation of average sizes of crystalline grains of the components in the nanocomposites.

The decrease in the crystallite sizes of the major phase upon the introduction of the second component is a general rule for all the considered nanocrystalline systems. The relative change in the crystalline grain sizes

$$d_{rel} = (d_0 - d)/d_0 \tag{7}$$

(d is the size of crystallites of a given phase in the nanocomposite, and d_0 is the size of crystallites of the pure oxide at the same annealing temperature) is determined by the properties of the major phase (Fig. 18). The char-
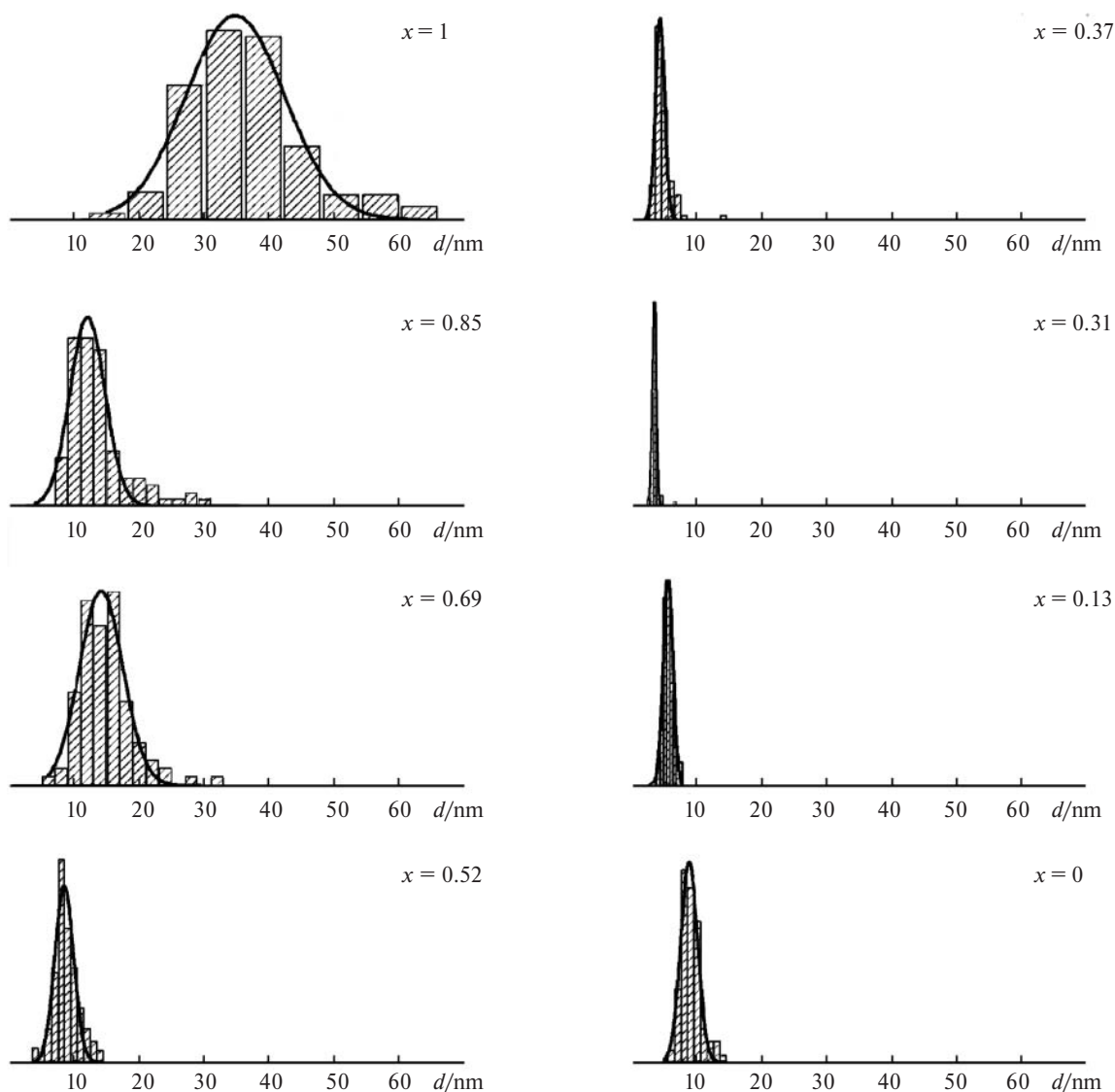

Fig. 16. Particle size distribution obtained by transmission electron microscopy for the SnO_2—Fe_2O_3 nanocomposites annealed at 500 °C.
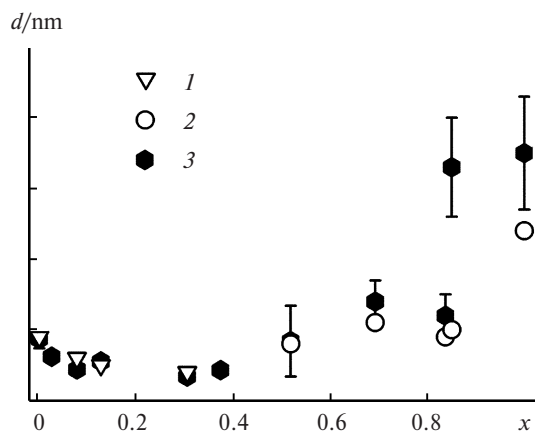
Fig. 17. Comparison of the CSR sizes of the main component in the $SnO_2-Fe_2O_3$ nanocomposites: $d_{XRD}(SnO_2)$ (*1*) and $d_{XRD}(Fe_2O_3)$ (*2*) and the particle sizes determined by transmission electron microscopy (d_{TEM}), $x = [Fe]/([Fe] + [Sn])$.

acter of changes in the sizes of the SnO_2 crystallites is independent of which of the oxides (Fe_2O_3, MoO_3, or V_2O_5) is the second component of the nanocomposite. The relative change in the crystallite size d_{rel} upon the introduction of the second component into the major phase increases in the series $V_2O_5 \approx MoO_3 < Fe_2O_3 < SnO_2$ (see Fig. 18). This tendency correlates with the increase in the Tamman temperature ($0.5T_m$) for these oxides

$$V_2O_5 \ (346 \ °C) < MoO_3 \ (398 \ °C) <$$
$$< Fe_2O_3 \ (783 \ °C) < SnO_2 \ (1000 \ °C).$$
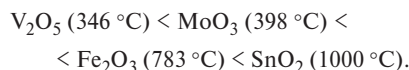
Thus, the smaller the mobility of ions of the crystalline lattice of the nanocomposite major phase the greater the effect of the second component on the rate of the crystalline grain growth in the matrix.
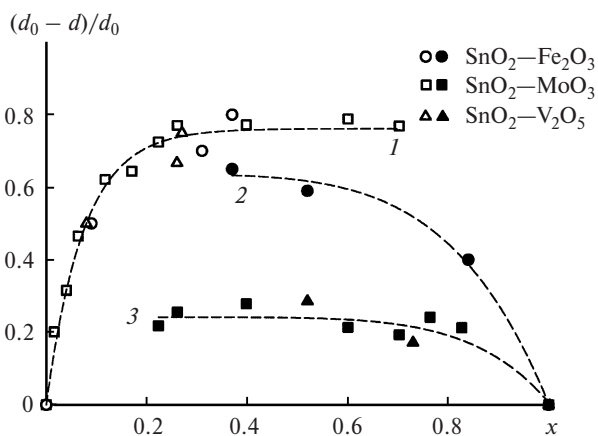

Fig. 18. Relative changes in the crystallite size in the $SnO_2-M_nO_m$ nanocomposites annealed at 500 °C: *1*, $d_{rel}(SnO_2)$ in various nanocomposites; *2*, $d_{rel}(Fe_2O_3)$ in $SnO_2-Fe_2O_3$; *3*, $d_{rel}(MoO_3)$ in SnO_2-MoO_3 and $d_{rel}(V_2O_5)$ in $SnO_2-V_2O_5$, $x = [M]/([M] + [Sn])$.

The specific surface area S_{sp} of the nanocomposites is determined by the conditions of synthesis: the method of the introduction of the second component and the annealing temperature.[18−21] In all cases, several regions can be distinguished in the plots of S_{sp} *vs* composition (Fig. 19). The single-phase region from the side of SnO_2 $0 \leq x \leq x_2$ (see Fig. 15) corresponds to the maximum S_{sp} values that increase with an increase in x due to a decrease in the SnO_2 particle size. The single-phase region from the side of M_nO_m ($x_3 \leq x \leq 1$) is characterized by the lowest S_{sp} values, which agrees with the large size of the M_nO_m particles. The two-phase region $x_2 < x < x_3$ corresponds to the intermediate S_{sp} values, and the specific surface decreases with an increase in x because of increasing the fraction and particle size of M_nO_m.

4. Acidic-basic and oxidation properties of the nanocomposites

A considerable contribution to the sensor signal is made by the acidic-basic and redox reactions that occur on the surface of the sensitive material upon the interaction with the gas phase. The specificity or selectivity of these reactions is primarily determined by the nature of the active sites on the surface. Let us consider the influence of the nanocomposite composition on the acidic and oxidation properties of the materials upon the interaction with the gas phase.

Hydroxy groups, chemisorbed oxygen, and coordinatively unsaturated atoms can act as active sites on the oxide surface.[48−50] The oxidation ability of the oxides is attributed[51] to chemisorbed oxygen and variable-valence metal atoms. In the second case, the efficiency of the charge transfer from the matrix to an active cation plays a great role.[52] Acid sites can be grouped as Brönsted (hydroxy groups) and Lewis (coordinatively unsaturated
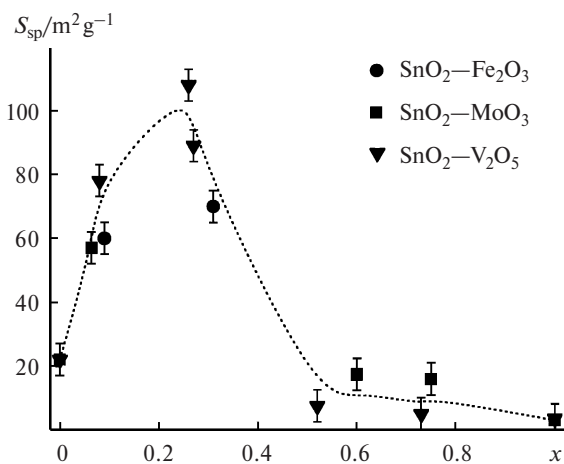

Fig. 19. Specific surface area S_{sp} *vs* composition of the nanocomposites annealed at 500 °C, $x = [M]/([M] + [Sn])$.

cations) sites. The strength of the Lewis acid sites can be related to the electronegativity of each element in the compound and to the q^2/r value, where q and r are the charge and radius of the corresponding cation, respectively. Higher values of the electronegativity and q^2/r ratio usually correspond to a greater strength of the acid site.[53] The strength of the conjugated base (oxygen of the crystalline lattice of the oxide) decreases with an increase in the acid site strength.

Thermal treatment exerts a substantial effect[54] on the acidic properties of the SnO$_2$ surface. The NH$_3$-TPD spectrum of tin dioxide annealed at 300 °C contains an intense peak at 136 °C (Fig. 20), which can be assigned to the desorption of ammonia bound to the surface hydroxy groups, *viz.*, Brönsted acid sites.[55] The peaks at 290 and 477 °C can be ascribed to ammonia desorption from the Lewis acid sites, which represent the coordinatively unsaturated Sn^{4+} cations with coordination numbers of 5 and 4, respectively.[56] The fraction of the strong acid sites increases with an increase in the annealing temperature to 700 °C. However, their total number calculated per 1 m^2 (A/S_{sp}) changes insignificantly. The disappearance of the Brönsted acid sites after calcination of the samples at 700 °C is explained by complete removal of the hydroxy groups from the sample surface. Subsequent increase in the annealing temperature decreases the specific surface area to 3—5 m^2 g^{-1}. In this case, no adsorption/desorption of ammonia was observed.
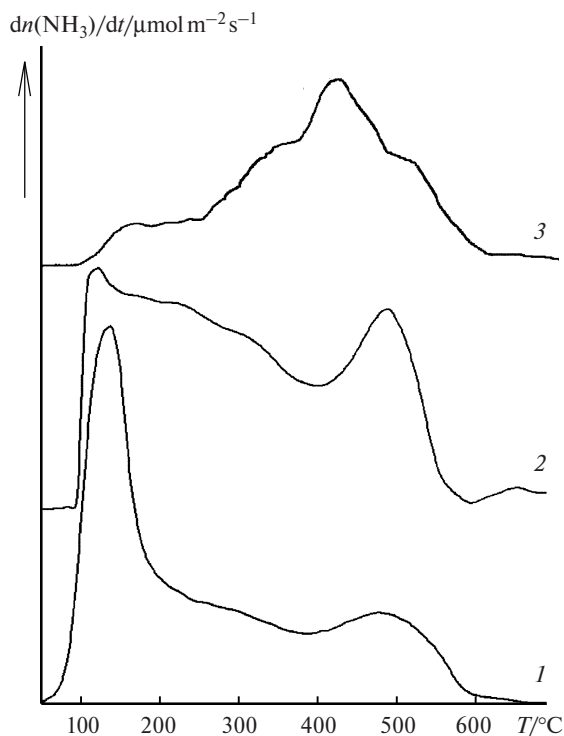
The peak at 250 °C in the NH$_3$-TPD spectrum of Fe$_2$O$_3$ (Fig. 21) can be assigned to NH$_3$ desorption from the Fe^{3+} surface cations, which are Lewis acid sites of medium strength.[57,58] The temperature of ammonia desorption from the acid sites, *vis.*, Sn^{4+} cations (290, 477 °C), is higher than that for desorption from the Fe^{3+} cations (250 °C), which correlates with the q^2/r value for Sn^{4+} (23.2) exceeding that for Fe^{3+} (14.0). In the SnO$_2$—Fe$_2$O$_3$ nanocomposites, the total amount of absorbed ammonia decreases with an increase in the Fe$_2$O$_3$ content. The addition of iron oxide decreases both the amount of physically adsorbed ammonia and the activation energy of desorption as follows from the shift of the peak maxima to lower temperatures. The appearance of the peak at $T = 350$ °C in the NH$_3$-TPD spectrum of the SnO$_2$—Fe$_2$O$_3$ nanocomposite ($x = 0.84$) can be attributed to ammonia desorption from the Sn^{4+} cations bound[29] to the Fe^{3+} surface cations. Ammonia desorption from the strong Lewis acid sites (at $T > 400$ °C) is observed only for pure SnO$_2$ and SnO$_2$ with small Fe$_2$O$_3$ content. Thus, the surface tin cations with a coordination number of 4 play the role of strong acid sites in the SnO$_2$—Fe$_2$O$_3$
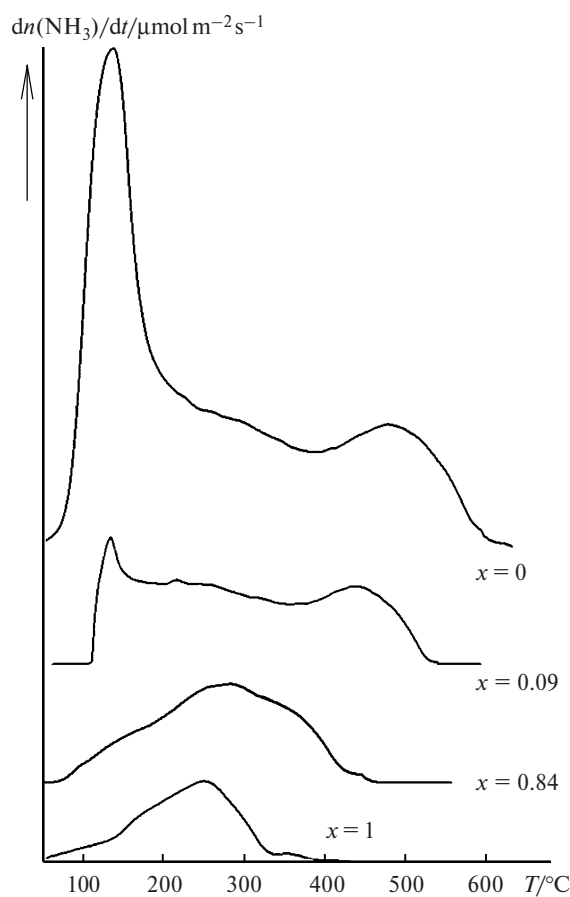
dn(NH$_3$)/dt/μmol m^{-2} s^{-1}

dn(NH$_3$)/dt/μmol m^{-2} s^{-1}

Fig. 20. Profiles of the temperature-programmed ammonia desorption (NH$_3$-TPD) of nanocrystalline SnO$_2$ annealed at 300 (*1*), 500 (*2*), and 700 °C (*3*).

Fig. 21. Profiles of the temperature-programmed ammonia desorption (NH$_3$-TPD) of the SnO$_2$—Fe$_2$O$_3$ nanocomposites annealed at 300 °C.

nanocomposites, and the segregation of the second oxide on the SnO_2 surface decreases their amount.

In the SnO_2—MoO_3 system, the maximum number of acid sites per 1 m^2 of the surface (A/S_{sp}) was found[54] for pure MoO_3. The maximum contribution to the total surface acidity is made, in this case, by the weak Brönsted sites, from which ammonia is desorbed at $T = 110$ °C (Fig. 22). The second intense peak at $T = 277$ °C can be assigned to the decomposition of a compound of the ammonium molybdate type. The low Lewis acidity of MoO_3 is due, most likely, to the partial decomposition of the crystallite surface with a decrease in the oxidation state of molybdenum accompanied by a decrease in the charge and an increase in the ion radius of the cations. A decrease in the MoO_3 content in the SnO_2—MoO_3 nanocomposites reduces the number of the weak acid sites and increases the fraction of the medium and strong Lewis acid sites (Sn^{4+}, Mo^{6+}, Mo^{5+}, and Mo^{4+}).[59]

The NH_3-TPD spectra of vanadium oxide and SnO_2—V_2O_5 nanocomposite with $x = 0.52$ exhibit two sharp intense peaks at 185 and 234 °C (Fig. 23), which can be ascribed only to the formation of chemical compounds of V_2O_5 with NH_3, because such a high value of

the total ammonia adsorption per surface unit exceeds the acceptable limit,[60—63] being 1—5 atom nm^{-2}. The peaks at 320—324 °C in the spectra of the SnO_2—V_2O_5 nanocomposites with $x = 0.52$ and 0.27 correspond to the Lewis acid sites of vanadium oxide. The broad peak in the spectrum of the SnO_2—V_2O_5 nanocomposite ($x = 0.27$) at $T = 166$ °C can be attributed to ammonia desorption from the Brönsted acid sites (hydroxy groups), which are bound to amorphous vanadium oxide segregated on the surface of the SnO_2 grains. The acid site concentration on the sample surface increases with an increase in the vanadium content in the nanocomposites.

The SnO_2—Fe_2O_3 nanocomposites are reduced[57] with hydrogen (H_2-TPR) at $T > 200$ °C (Fig. 24). The H_2-TPR spectrum of Fe_2O_3 contains two peaks at 363 and 534 °C, which are assigned to the reduction of Fe_2O_3 to Fe_3O_4 and Fe, respectively.[64] In the H_2-TPR spectrum, one peak at $T = 650$ °C corresponding to the reduction of SnO_2 to metallic tin is attributed to tin dioxide.[65,66] The SnO_2—Fe_2O_3 nanocomposite with $x = 0.84$ is characterized by the intense peak at $T = 568$ °C corresponding to
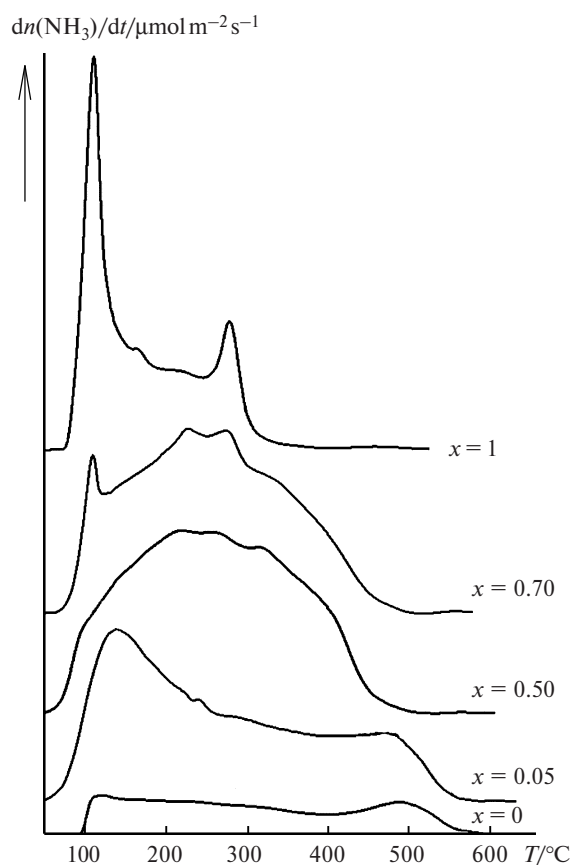

Fig. 22. Profiles of the temperature-programmed ammonia desorption (NH_3-TPD) of the SnO_2—MoO_3 nanocomposites annealed at 500 °C.
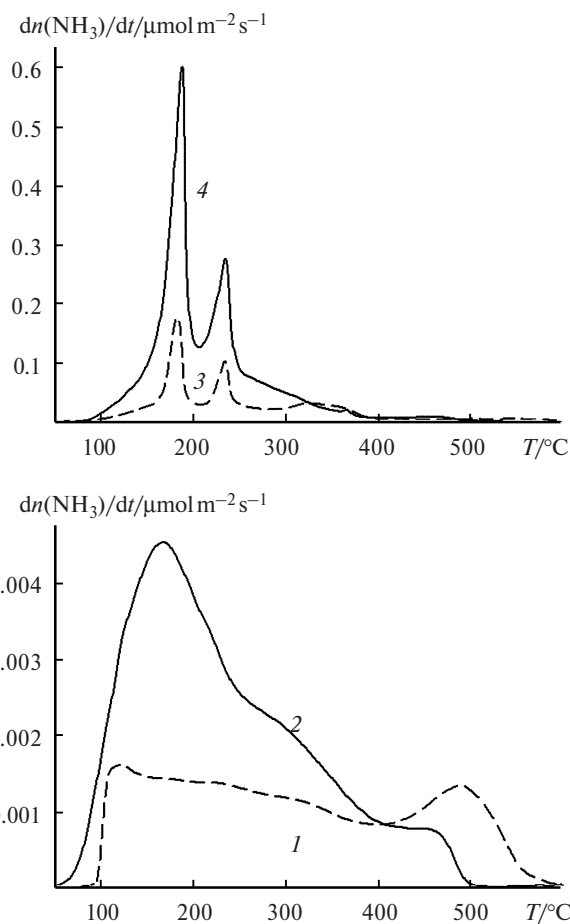

Fig. 23. Profiles of the temperature-programmed ammonia desorption (NH_3-TPD) of the SnO_2—V_2O_5 nanocomposites annealed at 500 °C; $x = 0$ (*1*), 0.27 (*2*), 0.52 (*3*), and 1.0 (*4*).
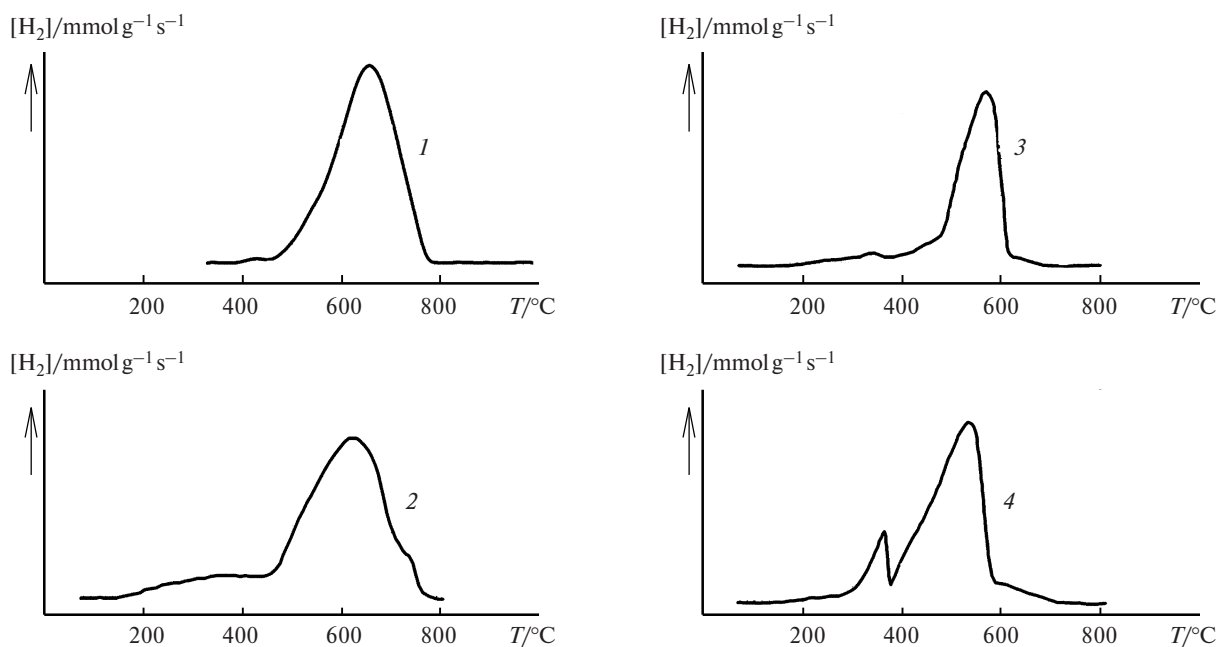
Fig. 24. Profiles of the temperature-programmed reduction with hydrogen (H$_2$-TPR) of the SnO$_2$—Fe$_2$O$_3$ nanocomposites annealed at 300 °C; $x = 0$ (*1*), 0.08 (*2*), 0.84 (*3*), and 1.0 (*4*).

the simultaneous reduction of tin oxide and iron oxide to the metals. The weak peak at 338 °C can be assigned to the incomplete reduction of Fe$_2$O$_3$ to Fe$_3$O$_4$. This peak is absent from the H$_2$-TPR spectrum of the SnO$_2$—Fe$_2$O$_3$ nanocomposite with $x = 0.08$. At the same time, the presence of a wide peak at 300—400 °C in the spectra of

the SnO$_2$—Fe$_2$O$_3$ nanocomposites with $x = 0.08$ and 0.84 indicates the reduction of Sn^{IV} to Sn^{II}, which is possible for amorphous tin oxides.[66]

The H$_2$-TPR spectrum of MoO$_3$ (Fig. 25) exhibits two peaks at 700 and 870 °C attributed to the reduction of MoO$_3$ to MoO$_2$ and Mo, respectively.[67] The introduc-
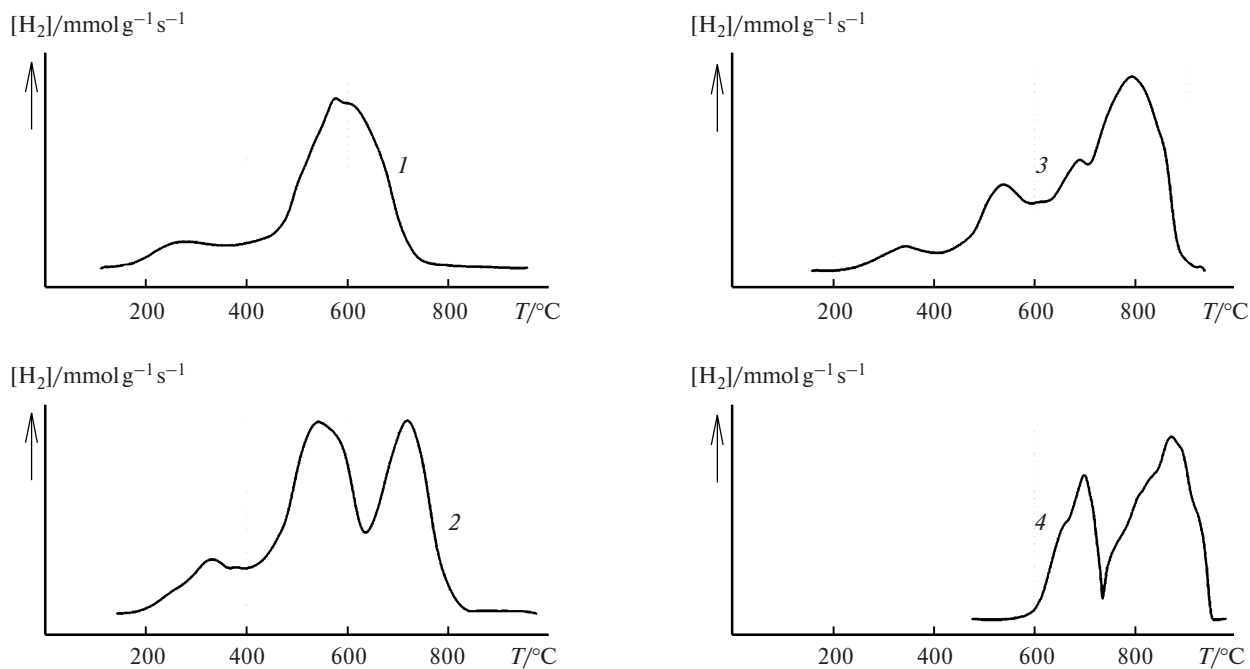

Fig. 25. Profiles of the temperature-programmed reduction with hydrogen (H$_2$-TPR) of the SnO$_2$—MoO$_3$ nanocomposites annealed at 500 °C; $x = 0.05$ (*1*), 0.50 (*2*), 0.70 (*3*), and 1.0 (*4*).

tion of a small amount of molybdenum into tin dioxide ($x = 0.05$) results in the shift of the peak of SnO_2 reduction to lower temperature and the appearance of a broad peak at 200—300 °C corresponding[68] to the reduction of the $\beta\text{-}MoO_3$ segregation on the SnO_2 crystallite surface. The H_2-TPR spectra of the $SnO_2\text{—}MoO_3$ nanocomposites with $x = 0.5$ and 0.7 represent the superposition of the spectra of SnO_2 and MoO_3 reduction. In all cases, the introduction of the second component decreases the temperature of reduction of both SnO_2 and MoO_3 in the nanocomposites as compared to the pure oxides.

An analysis of the experimental data obtained for the $SnO_2\text{—}M_nO_m$ systems ($M_nO_m = Fe_2O_3$, MoO_3, V_2O_5) makes it possible to reveal the following main regularities.

1. The total number of acid sites on the nanocomposite surface decreases with an increase in the Fe content in the $SnO_2\text{—}Fe_2O_3$ nanocomposites and, on the contrary, increases with an increase in x in the $SnO_2\text{—}MoO_3$ and $SnO_2\text{—}V_2O_5$ nanocomposites (Fig. 26). This correlates with the change in the q^2/r value in the series Fe^{3+} (14.0) < Sn^{4+} (23.2) < V^{5+} (46.3) < Mo^{6+} (60.0). However, the increase in the total acidity of the surface in the $SnO_2\text{—}MoO_3$ and $SnO_2\text{—}V_2O_5$ nanocomposites is caused by an increase in the number of the Brönsted acid sites, and the contribution of the Lewis acid sites to the total acidity decreases.

2. The decrease in the reduction temperature of the nanocomposite components as compared to the individual oxides, most likely, has a general character and indicates the higher oxidation ability of the nanocomposites, which agrees with the data[65,69] for the Sn—Fe—O and Sn—Mo—O catalysts. This can be due to the high imperfection of the solid solution surface for the heterovalent substitution and formation of highly defect segregations of the second component on the surface of the major phase crystallites.
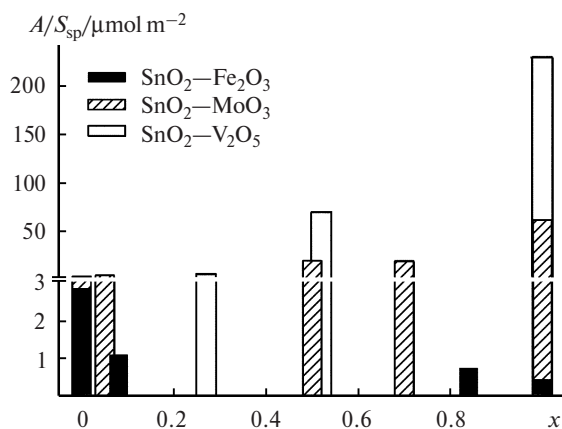
5. Sensor properties of nanocomposites

Let us analyze the sensor properties[19,21,40,54,57] of the $SnO_2\text{—}Fe_2O_3$, $SnO_2\text{—}V_2O_5$, and $SnO_2\text{—}MoO_3$ nanocomposites. The gases that are detected were NH_3 (typical Lewis base) and EtOH (the molecule with both donor and acceptor functional groups).

5.1. Detection of NH_3. The dependence of the sensor signal (S) towards NH_3 *vs* nanocomposite composition is shown in Fig. 27. In the $SnO_2\text{—}MoO_3$ and $SnO_2\text{—}V_2O_5$ systems, the S value changes nonmonotonically with an increase in x. The maximum S values correspond to the composition range $0.25 < x < 0.55$. The monotonic decrease in the sensor signal with an increase in the iron content is observed for the $SnO_2\text{—}Fe_2O_3$ nanocomposites.

To compare the acidic properties of the nanocomposites[54,57] and their sensor signal towards NH_3, we estimated the number of sites (per 1 m^2 of the surface area of the sample) with an activation energy of ammonia desorption of 130—150 kJ mol^{-1}, which corresponds[22] to the temperature interval 300—500 °C optimal for ammonia detection.

For all the considered systems, the sensor signal value increases monotonically with an increase in the number of the corresponding acid sites (Fig. 28). Thus, ammonia chemisorption on the Lewis acid sites with the charge transfer from the NH_3 molecule to the oxide surface[56] is the main factor responsible for the conductivity change.

5.2. Detection of EtOH. For the interaction with ethanol vapor, the $SnO_2\text{—}Fe_2O_3$ nanocomposites demonstrate similar dependences of the number of acid sites and sensor signal on the sample composition. These dependences have an opposite character for the $SnO_2\text{—}V_2O_5$ and $SnO_2\text{—}MoO_3$ systems: an increase in the total acidity with an increase in x is accompanied by a decrease in the sensor signal towards ethanol[19,40,55] (Fig. 29).
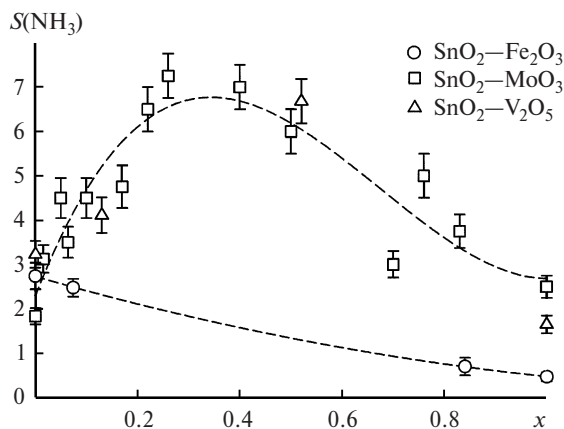
Fig. 26. Total number of acid sites per 1 m^2 of the nanocomposite surface, $x = [M]/([M] + [Sn])$.

Fig. 27. Sensor signals from the nanocomposites towards 500 ppm NH_3 at 350 °C, $x = [M]/([M] + [Sn])$.
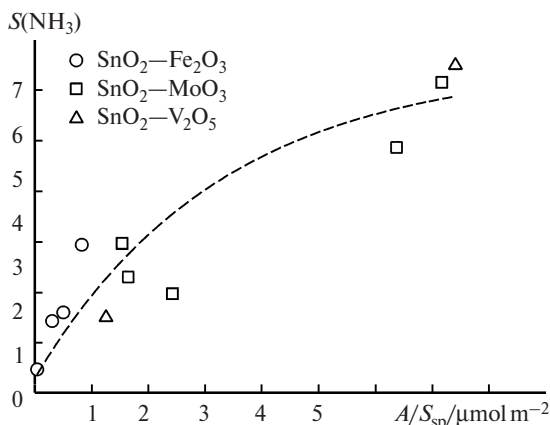
Fig. 28. Sensor signals from the nanocomposites towards NH$_3$ at different amounts of acid sites (A/S_{sp}) from which ammonia desorbs in the temperature interval 300—500 °C.

The interaction of ethanol with the oxide surface is a complicated process and the sensor signal value depends on both the number of adsorption sites on the sample surface and their nature. There are two main mechanisms of ethanol conversion: dehydration and oxidative dehydrogenation.[70] The former mechanism mainly occurs on the surface containing the Brönsted acid sites and results in a low sensor response. On the contrary, the dehydrogenation mechanism requires pairs of the Lewis acid and base sites to occur.[71] This type of interaction is accompanied by a change in the electroconductivity of the material due to the reaction with chemisorbed oxygen O$_s^-$

$$EtOH + O_s^- \rightarrow MeCHO + H_2O + e^-. \qquad (8)$$
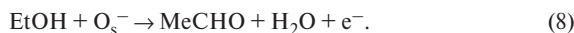
Coordinatively unsaturated metal cations and chemisorbed oxygen species are the Lewis acid and base sites, respectively, on the nanocomposite surface. Thus, in the case of the equal adsorption ability of the samples, the selectivity of ethanol conversion to acetaldehyde and the
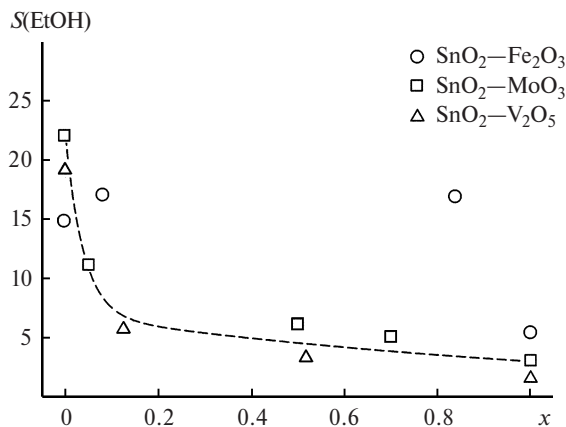
sensor signal value depend on the ratio between the strong (Lewis) and weak (Brönsted) acid sites. Ethanol dehydrates to C$_2$H$_4$ on the surface containing mainly the Brönsted sites, and these materials possess low sensitivity to alcohols. On the contrary, the samples with the predominant Lewis sites on the surface demonstrate a great response towards EtOH due to the conversion that occurs through dehydrogenation.

The Brönsted (A_B) and Lewis (A_L) acidity of the nanocomposite surface can be characterized by the number of acid sites per 1 m^2 of the sample surface from which ammonia desorbs in temperature intervals of 25—200 and 350—600 °C, respectively. For all series of the nanocomposites, the sensor response towards ethanol correlates with the ratio between the Lewis and Brönsted acidity of the surface A_L/A_B (Fig. 30).

The study of ethanol oxidation on the surface of the individual oxides SnO$_2$ and Fe$_2$O$_3$ and the SnO$_2$—Fe$_2$O$_3$ nanocomposites with $x = 0.08$ and 0.84 showed that acetaldehyde was the major oxidation product.[57] Ethyl acetate, ethylene, diethyl ether, acetic acid, and traces of acetone were also found (Fig. 31). An increase in the iron content in the samples leads to a decrease in the ethyl acetate and acetic acid content in the oxidation products and an increase in the amount of acetaldehyde and complete oxidation products (CO$_2$, H$_2$O). Pure Fe$_2$O$_3$ is characterized by a lower catalytic activity than the nanocomposite with $x = 0.84$, which can be due to its low specific surface area.

The conversion of ethanol at 200 °C is insignificant but increases sharply with temperature (Fig. 32). The conversion reaches 100% at 300 °C for the iron-containing samples and at 400 °C for pure SnO$_2$. Thus, the nanocomposites manifest higher catalytic activity in ethanol oxidation than the individual oxides, which is well consistent with the H$_2$-TPR data. From the viewpoint of the sensor properties, this results in a decrease in the temperature corre-
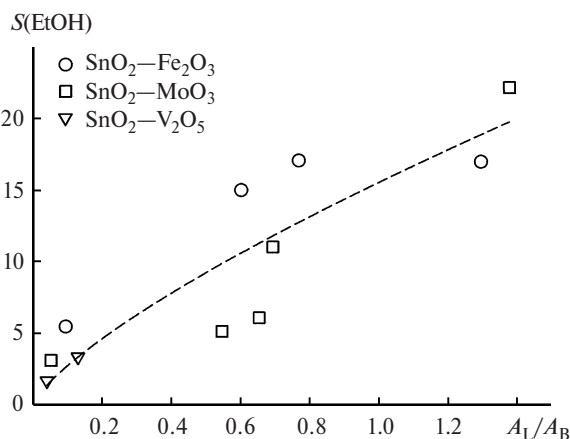

Fig. 29. Sensor signals from the nanocomposites towards 1 µL of EtOH at 275 °C, $x = [M]/([M] + [Sn])$.

Fig. 30. Sensor signals from the nanocomposites towards ethanol at different ratios of the number of Lewis (A_L) to Brönsted (A_B) acid sites.
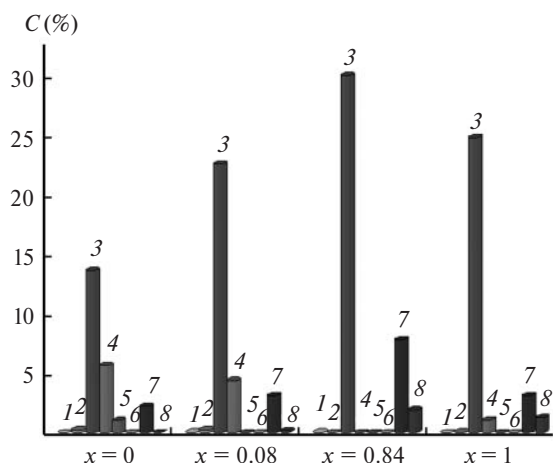
Fig. 31. Ethanol conversion products on the SnO_2—Fe_2O_3 nanocomposite surface at 250 °C: CH_4 (*1*), C_2H_4 (*2*), MeCOH (*3*), EtOAc (*4*), MeCOOH (*5*), CO (*6*), CO_2 (*7*), and other (*8*); here and in Fig. 32, *C* is the degree of conversion.

sponding to the maximum sensor signal. In addition, the temperature at which the maximum sensor signal is observed (Fig. 33) corresponds to the temperature of complete ethanol conversion determined in catalytic experiments.

Conclusion

The studies performed showed correlations between the catalytic activity and sensor properties of the nanocrystalline oxide materials. The modification of the semiconducting oxides by the catalysts allows one to control the type and density of acid sites and the redox properties of the surface and to thus enhance the selectivity of the materials.

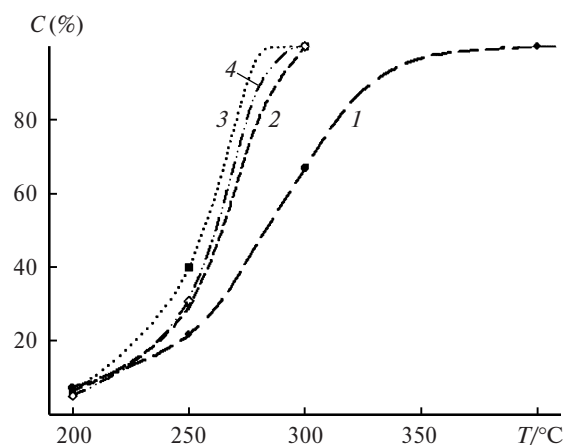The mutual distribution of components between the surface and bulk of crystallites in the SnO_2—M_nO_m

Fig. 32. Temperature plots of the ethanol conversion on the surface of SnO_2, Fe_2O_3, and the SnO_2—Fe_2O_3 nanocomposites: $x = 0$ (*1*), 0.08 (*2*), 0.84 (*3*), and 1.0 (*4*).
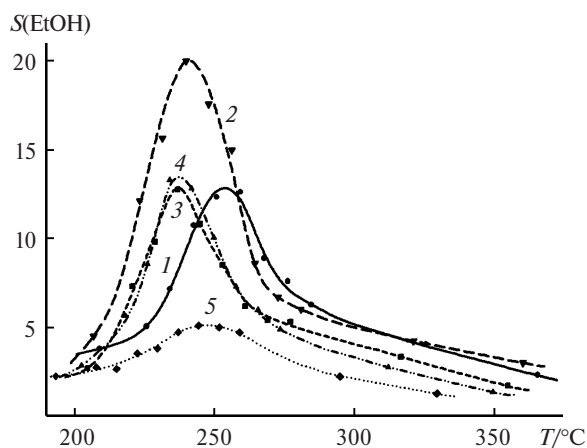
Fig. 33. Temperature plots of the sensor signal from the SnO_2—Fe_2O_3 nanocomposites with $x = 0$ (*1*), 0.03 (*2*), 0.08 (*3*), 0.84 (*4*), and 1.0 (*5*) towards 1 µL of EtOH.

nanocrystalline systems is complicated. It is shown that the regions of existence of solid solutions and conditions of phase formation in these systems depend substantially on the dispersity of the samples.

Since the particles are small, nanocrystalline systems should be characterized using mutually supplementing methods: together with X-ray diffraction, important information on the structure of these systems can be obtained by scanning electron microscopy, electron diffraction, Raman spectroscopy, and Mössbauer spectroscopy.

References

1. M. Batzill, U. Diebold, *Prog. Surf. Sci.*, 2005, **79**, 47.
2. D. S. Ginley, C. Bright, *Mater. Res. Soc. Bull.*, 2000, **25**, 15.
3. X. Wang, Y. Xie, *Catal. Lett.*, 2001, **75**, 73.
4. J. H. Grimm, D. G. Bessarabov, U. Simon, R. D. Sanderson, *J. Appl. Electrochem.*, 2000, **30**, 293.
5. A.-M. Popescu, S. Mihaiu, S. Zuca, *Z. Naturforsch.*, 2002, **57a**, 71.
6. N. Yamazoe, *Sens. Actuators, B*, 2005, **108**, 2.
7. W. Gopel, K. D. Schierbaum, *Sens. Actuators, B*, 1995, **26—27**, 1.
8. N. Barsan, M. Schweizer-Berberich, W. Gopel, *Fresenius J. Anal. Chem.*, 1999, **365**, 287.
9. K. Takahata, in *Chemical Sensor Technology*, Ed. T. Seiyama, Elsevier, Amsterdam, 1988, p. 39.
10. E. Souteyrand, in *Les Capteurs Chimiques*, Ed. C. Pijolat, CMC2, Ecole Centrale de Lyon, Lyon, 1997, p. 52.
11. F. F. Vol´kenshtein, *Elektronnaya teoriya kataliza na poluprovodnikakh* [*Electronic Theory of Catalysis on Semiconductors*], Fizmatgiz, Moscow, 1960, 188 pp. (in Russian).
12. H. Idriss, M. A. Barteau, *Adv. Catal.*, 2000, **45**, 261.
13. A. Cimino, F. S. Stone, *Adv. Catal.*, 2002, **47**, 141.

14. H.-J. Freund, M. Bäumer, H. Kuhlenbeck, *Adv. Catal.*, 2000, **45**, 333.

15. S. M. Kudryavtseva, A. A. Vertegel, S. V. Kalinin, N. N. Oleynikov, L. I. Ryabova, L. L. Meshkov, S. N. Nesterenko, M. N. Rumyantseva, A. M. Gaskov, *J. Mater. Chem.*, 1997, **7**, 2269.

16. O. Safonova, I. Bezverkhy, P. Fabritchny, M. Rumyantseva, A. Gaskov, *J. Mater. Chem.*, 2002, **12**, 1174.

17. M. N. Rumyantseva, O. V. Safonova, M. N. Bulova, L. I. Ryabova, A. M. Gas´kov, *Izv. Akad. Nauk, Ser. Khim.*, 2003, **52**, 1151 [*Russ. Chem. Bull., Int. Ed.*, 2003, **52**, 1217].

18. M. N. Rumyantseva, V. V. Kovalenko, A. M. Gaskov, T. Pagnier, D. Machon, J. Arbiol, J. R. Morante, *Sens. Actuators, B*, 2005, **109**, 64.

19. E. A. Makeeva, M. N. Rumyantseva, A. M. Gas´kov, *Izv. Akad. Nauk, Neorgan. Mater.*, 2005, **41**, 442 [*Inorg. Mater.,* 2005, **41**, 370 (Engl. Transl.)].

20. M. N. Rumyantseva, A. M. Gaskov, N. Rosman, T. Pagnier, J. R. Morante, *Chem. Mater.*, 2005, **17**, 893.

21. V. V. Kovalenko, Ph. D. (Chem.) Thesis, M. V. Lomonosov Moscow State Univ., Moscow, 2006, 127 pp. (in Russian).

22. V. V. Yushchenko, *Zh. Fiz. Khim.*, 1997, **71**, 628 [*Russ. J. Phys. Chem.*, 1997, **71** (Engl. Transl.)].

23. R. D. Shannon, C. T. Prewitt, *Acta Crystallogr., Sect. B*, 1969, **25**, 925.

24. C. Djega-Mariadassou, F. Basile, P. Poix, A. Michel, *Ann. Chim.*, 1973, **8**, 15.

25. F. H. Chung, *J. Appl. Crystallogr.*, 1974, **7**, 526.

26. Y.-C. Xie, Y.-Q. Tang, *Adv. Catal.*, 1990, **37**, 1.

27. V. V. Kovalenko, M. N. Rumyantseva, P. B. Fabritchnyi, A. M. Gaskov, *Mendeleev Commun.*, 2004, **14**, 140.

28. S. R. Davis, A. V. Chadwick, J. D. Wright, *J. Phys. Chem. B*, 1997, **101**, 9901.

29. L. Abello, B. Bochu, A. Gaskov, S. Koudryavtseva, G. Lucazeau, M. Rumyantseva, *J. Solid State Chem.*, 1998, **135**, 78.

30. M. Boulova, A. Galerie, A. Gaskov, G. Lucazeau, *Sens. Actuators, B*, 2000, **71**, 134.

31. P. B. Fabrichnyi, A. M. Babeshkin, A. N. Nesmeyanov, V. N. Onuchak, *Fiz. Tverd. Tela*, 1970, **12**, 2032 [*Sov. Phys. Sol. State*, 1970, **12** (Engl. Transl.)].

32. P. B. Fabritchnyi, A. M. Babeshkin, A. N. Nesmeianov, *J. Phys. Chem. Solids*, 1971, **32**, 1701.

33. P. B. Fabritchnyi, E. V. Lamykin, A. M. Babeshkin, A. N. Nesmeianov, *Solid State Commun.*, 1972, **11**, 343.

34. V. V. Berentsveig, Z. A. Hasan, P. B. Fabritchnyi, T. M. Ivanova, A. P. Rudenko, *React. Kinet. Catal. Lett.*, 1980, **15**, 239.

35. W. Kündig, H. Bömmel, G. Constabaris, R. H. Lindquist, *Phys. Rev.*, 1966, **142**, 327.

36. D. A. Khramov, V. S. Urusov, *Izv. Akad. Nauk, Neorg. Mater.* [*Izv. Acad. Sci. USSR, Inorganic Materials*], 1983, **19**, 1880 (in Russian).

37. S. Ichiba, T. Yamaguchi, *Chem. Lett.,* 1984, **13**, 1681.

38. F. Schneider, K. Melzer, H. Mehner, G. Dehe, *Phys. Stat. Sol. (a)*, 1977, **39**, K115.

39. F. J. Berry, C. Greaves, J. G. McManus, M. Mortimer, G. Oates, *J. Solid State Chem.*, 1997, **130**, 272.

40. J. Arbiol, J. R. Morante, P. Bouvier, T. Pagnier, E. Makeeva, M. Rumyantseva, A. Gaskov, *Sens. Actuators, B*, 2006, **118**, 156.

41. F. Harb, B. Gerand, G. Nowogrocki, M. Figlarz, *Solid State Ionics*, 1989, **32—33**, 84.

42. M. S. Moreno, R. F. Egerton, P. A. Midgley, *Phys. Rev., B*, 2004, **69**, 233304/1.

43. M. S. Moreno, R. F. Egerton, J. J. Rehr, P. A. Midgley, *Phys. Rev., B*, 2005, **71**, 035103/1.

44. D. Wang, D. S. Su, R. Schlögl, *Z. Anorg. Allg. Chem.*, 2004, **630**, 1007.

45. G.-J. Li, X.-H. Zhang, S. Kawi, *Sens. Actuators, B*, 1999, **60**, 64.

46. H. Gleiter, *Acta Mater.*, 2000, **48**, 1.

47. N. L. Wu, S.-Y. Wang, I. A. Rusakova, *Science*, 1999, **285**, 1375.

48. A. A. Tsyganenko, D. V. Pozdnyakov, V. N. Filimonov, *J. Mol. Struct.*, 1975, **29**, 299.

49. I. E. Wachs, J.-M. Jehng, W. Ueda, *J. Phys. Chem., B*, 2005, **109**, 2275.

50. C. Morterra, M. P. Mentruit, G. Cerrato, *Phys. Chem. Chem. Phys.*, 2002, **4**, 676.

51. B. M. Reddy, K. Narsimha, C. Sivaraj, P. K. Rao, *Appl. Catal.*, 1989, **55**, Ll.

52. P. J. Pomonis, J. C. Vickerman, *Faraday Discuss. Chem. Soc.*, 1981, **71**, 247.

53. K. Chen, A. T. Bell, E. Iglesia, *J. Phys. Chem., B*, 2000, **104**, 1292.

54. V. V. Kovalenko, A. A. Zhukova, M. N. Rumyantseva, A. M. Gaskov, V. V. Yushchenko, I. I. Ivanova, T. Pagnier, *Sens. Actuators, B*, 2007, **126**, 52.

55. V. A. Burmistrov, *Gidratirovannye oksidy IV i V grupp* [*Hydrated Oxides of IV and V Groups*], Nauka, Moscow, 1986, 160 pp. (in Russian).

56. M. W. Abee, D. F. Cox, *Surf. Sci.*, 2002, **520**, 65.

57. M. Rumyantseva, V. Kovalenko, A. Gaskov, E. Makshina, V. Yushchenko, I. Ivanova, A. Ponzoni, G. Faglia, E. Comini, *Sens. Actuators, B*, 2006, **118**, 208.

58. G. Ramis, M. A. Larrubia, G. Busca, *Top. Catal.,* 2000, **11/12**, 161.

59. E. M. Gaigneaux, S. R. G. Carrazan, P. Ruiz, B. Delmon, *Thermochim. Acta*, 2002, **388**, 27.

60. F. Okada, A. Satsuma, A. Furuta, A. Miyamoto, T. Hattori, Y. Murakami, *J. Phys. Chem.*, 1990, **94**, 5900.

61. M. Niwa, Y. Habuta, K. Okumura, N. Katada, *Catal. Today*, 2003, **87**, 213.

62. Y. Habuta, N. Narishige, K. Okumura, N. Katada, M. Niwa, *Catal. Today*, 2003, **87**, 131.

63. M. Ai, *J. Catal.*, 1975, **40**, 318.

64. H.-Y. Lin, Y.-W. Chen, C. Li, *Thermochim. Acta*, 2003, **400**, 61.

65. X. Wang, Y.-C. Xie, *React. Kinet. Catal. Lett.*, 2001, **72**, 229.

66. P. W. Park, H. H. Kung, D.-W. Kim, M. C. Kung, *J. Catal.*, 1999, **184**, 440.

67. P. Arnoldy, J. C. M. De Jonge, J. A. Moulijn, *J. Phys. Chem.*, 1985, **89**, 4517.

68. F. Goncalves, P. R. S. Medeiros, J. G. Eon, L. G. Appel, *Appl. Catal., A*, 2000, **193**, 195.

69. N. G. Valente, L. A. Arrua, L. E. Cadus, *Appl. Catal., A*, 2001, **205**, 201.

70. T. Jinkawa, G. Sakai, J. Tamaki, N. Miura, N. Yamazoe, *J. Mol. Catal., A*, 2000, **155**, 193.

71. H. Idriss, E. G. Seebauer, *J. Mol. Catal., A*, 2000, **152**, 201.